Utrecht University

Performance study of the FoCal prototype detector using a 2.0 - 5.4 GeV pure positron beam

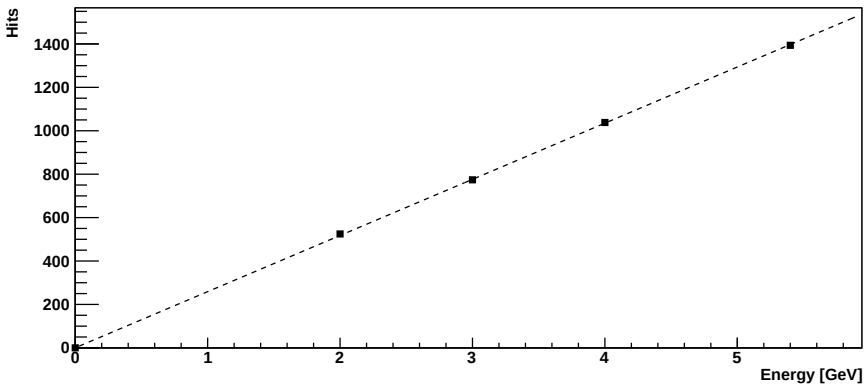

Author:
Martijn Dietze
Student number: 3861031

Supervisors:
Dr. ir. G.J.L. Nooren
Dr. E. Rocco

Bachelor research project at the Institute for Subatomic Physics

June 18, 2014

Abstract

This research commenced by preparing the Forward Calorimeter (FoCal) prototype detector for measurements on a 2.0 - 5.4 GeV pure positron beam at DESY, Hamburg. At beam energies of 2.0, 3.0, 4.0, and 5.4 GeV, enough data has been collected to achieve reasonable statistics. Additionally, data with 3 different threshold settings for the sensors has been collected at 2 GeV. During the first analysis of the data it was found that series of neighboring pixels in the sensors seemingly randomly turned on in multiple frames. Because of this effect (and other problems, such as synchronization errors), the detector has an undesired instability in time.

The first part of this thesis is focused on the investigation of said problems. The sections in the sensors that were found to have complications, have been masked in further analysis. In the second part, the energy resolution, longitudinal profile and linearity of the detector were checked to quantify the effects of the masking procedure. It was found that the energy resolution got worse for the 2.0 , 3.0 and 4.0 GeV data, but improved for the 5.4 GeV data. The linearity of the detector was found to be better with the masked data. Furthermore, the influence of the threshold settings has been determined. It was found that the low-threshold settings had the best energy resolution and the highest clustersize; the high-threshold settings had the highest signal-to-noise ratio. There are still multiple problems with the hardware, such as hot channels, synchronization errors and an inefficiency in the trigger system, that have not been dealt with in this work.

Contents

Chapter 1

Introduction

The FoCal prototype detector is a high-granularity digital electromagnetic sampling calorimeter which is designed to measure the energy of a single charged particle entering the detector. The number of particles measured by the detector is directly proportional to the energy of the entering particle, which makes this detector a good instrument to measure both energy and shower shape. The FoCal prototype detector has been built to investigate the possibility of adding a FoCal detector to the ALICE-detector (Fig. 1.1) at CERN, Geneva as part of a major upgrade. The FoCal detector should allow to discriminate direct photons from the decay of neutral pions in a large momentum range.

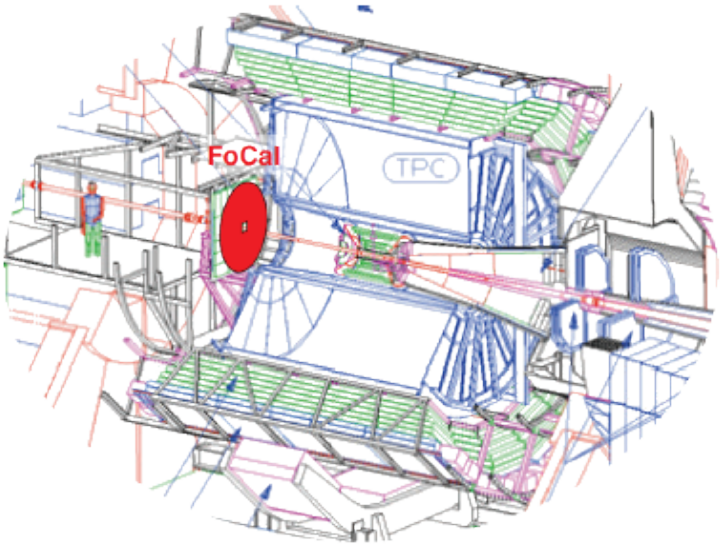

Figure 1.1: The position of the FoCal detector at ALICE. From [1].

This thesis will start with an overview of the theory required to understand the basic concepts behind the FoCal prototype detector in Chapter 2. The design of the detector and some parts of the software currently used will be discussed in Chapter 3. Chapter 4 will cover the preparations and the measurements on the test beam at DESY, Hamburg. Chapter 5 will discuss the problems found in the hardware and how some of these problems were resolved. Subsequently, the masked data is used for further analysis in Chapter 6. The impact of different threshold settings for the sensors is investigated in this chapter as well. Finally, the results are summarized and recommendations for future work are provided in Chapter 7 and 8, respectively.

Chapter 2

Theory

This chapter is used to give an overview of some of the concepts which are essential to the understading of the functioning of the FoCal prototype detector. The origin of cosmic radiation is discussed first, followed by the basic theory behind electromagnetic interactions and, at last, a description on the main components of electromagnetic detectors is given.

2.1 Cosmic radiation

Cosmic rays are primarily composed of protons and atomic nuclei. The primary source of these cosmic rays are supernovae. Cosmic muons are created when high energy primary cosmic rays interact with the Earth's atmosphere. When this interaction occurs, multiple particles are created, including: pions, kaons and nucleons. The charged pions can interact further with the atmosphere, but, in most cases, they will decay into muons. This process is illustrated in Fig. 2.1.

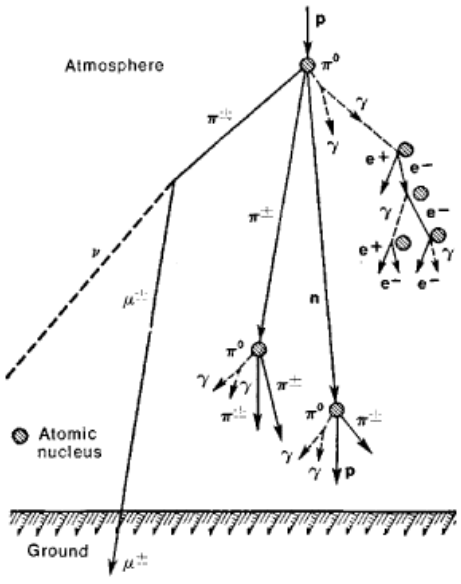

Figure 2.1: Illustration of the collisions in the atmosphere created by an incoming cosmic ray. p are protons, π pions, e^- electrons, e^+ positrons, γ photons, ν neutrinos and μ muons. From [2].

Because of the high energy of the muons, relativistic effects are important. The cosmic muons can, even though their lifetime is very short, reach the surface of the Earth, because of time dilation. The mean energy of these cosmic muons at sea level is on the order of a few GeV's.

2.2 Interactions with matter

Particles can interact with matter in various ways. To study these interactions, classifications of different types of particles have to be made. The first group of particles we will distinguish is the collection of neutral particles (e.g. neutral pions and kaons). These particles will only interact through the nuclear interactions. The second group is the collection of heavy charged particles (e.g. protons, charged pions and muons), which interact primarily through electromagnetic interactions. The third group is composed of light charged particles (e.g. electrons and positrons), which can lose a large fraction of their energy through radiation, in addition to electromagnetic radiation (Fig. 2.2). The fourth and last group is composed of photons.

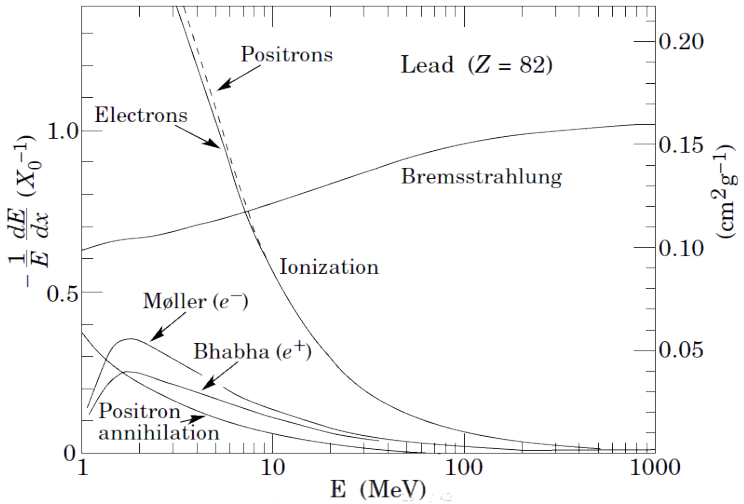

Figure 2.2: The fraction of energy loss per radiation length in lead as a function of the electron or positron energy. From [3].

The nuclear interaction is the primary interaction of these particles at low energies. However, at the energies we are looking at, this effect is very small and thus nuclear interactions will not be covered here. In the rest of this section, the focus will be on the electromagnetic interactions.

2.2.1 Heavy charged particles

In Fig. 2.3, an overview of the stopping power for positive muons in copper has been drawn as a function of the kinetic energy of the muons. It is clear that multiple energy-regions can be distinguished. In the first region, nuclear interactions are the primary interactions, which is followed by the Bethe-Bloch region (which has boundaries of $\approx$ 100 keV - 50 GeV, for muons in copper) and the last region is radiation dominated.

At a certain kinetic energy, an ionization minimum occurs. The energy loss below this minimum is proportional to $\frac{1}{v^2}$, which means the energy loss increases when the particle slows down. Above the minimum, the energy loss flattens out, until radiative effects become important. This minimum is also marked in Fig. 2.3.

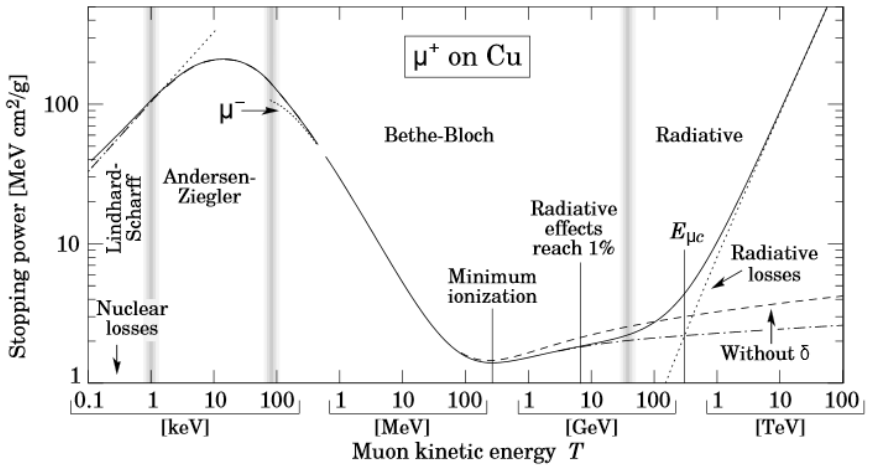

Figure 2.3: The stopping power for positive muons in copper as a function of its kinetic energy T. Vertical bands indicate boundaries between different theoretical approximations or dominant physical processes. From [3].

Elastic scattering and inelastic collisions

Charged particles moving through matter can interact with the bound electrons of the material. These interactions will give rise to either excitation (the energy level of the bound electron is lifted) or ionization (the bound electron is ejected from the atom). The energy of the particle moving through the material will be lowered by these effects. The rate of this energy loss is given by the Bethe-Bloch formula (Eq. 2.1 [4]). In this formula the approximation m $\gg$ m_e has been used.

$$-\left\langle \frac{dE}{dx} \right\rangle = 4\pi N_0 r_e^2 m_e c^2 z^2 \frac{Z}{A} \frac{1}{\beta^2} \left[\frac{1}{2} \ln\left(2m_e c^2 \beta^2 \gamma^2 \frac{T_{max}}{I^2}\right) - \beta^2 - \frac{\delta(\beta\gamma)}{2} - \frac{C}{Z} \right] \quad (2.1)$$

where

- N_0 the Avogadro number
- e the elementary charge
- ϵ_0 the permittivity of free space
- c the speed of light
- $r_e = \frac{e^2}{4\pi\epsilon_0 m_e c^2}$ the classical electron radius
- m_e the electron mass
- z the charge of particle
- Z the atomic number of the absorber material
- A the atomic mass of the absorber material
- v the speed of the incoming particle
- $\beta = \frac{v}{c}$ the speed per speed of light
- $\gamma = \frac{1}{\sqrt{1-\beta^2}}$ the Lorentz factor
- M the mass of the incoming particle
- $T_{max} = \frac{2m_e c^2 \beta^2 \gamma^2}{1+2\frac{m_e}{M}\sqrt{1+\beta^2\gamma^2}+\left(\frac{m_e}{M}\right)^2}$ the maximum transferable kinetic energy
- I the ionization potential
- $\delta(\beta\gamma)$ the correction to the density effect in the high energy region
- C the correction for atomic binding in the low energy region.

The Bethe-Bloch formula describes the energy loss per distance travelled for particles traversing matter. The terms in Eq. 2.1 show that the amount of energy loss is dependent on the material used as absorber. Generally, the highest energy loss (or stopping power) is achieved for the material with the highest density. The equation also shows that the rate of energy loss does not depend on the mass of the ionizing particle; only on its velocity and charge.

Radiation interactions

Since the cosmic muons have energies in the order of a few GeV's, radiation effects will be small (see Fig. 2.3) and thus these effects will not be discussed here.

2.2.2 Light charged particles

It has already been shown that the strength of the different interactions with matter has a strong dependency on the energy of the particle. For electrons, one can specify two regions (ignoring the nuclear interactions region): the ionization dominated region ($\mathrm{E} < \mathrm{E}_c$) and the radiation dominated region ($\mathrm{E} > \mathrm{E}_c$), where E_c can be approximated by: $\mathrm{E}_c \approx \frac{600\ \mathrm{MeV}}{\mathrm{Z}}$, with Z the charge number of the absorber's atoms [5]. In the ionization region, the treatment of electrons is almost the same as that of heavy charged particles; only a few adjustments have to be made. These adjustments are discussed below.

Elastic scattering and inelastic collisions

Eq. 2.1 holds for heavy charged particles which have a mass much higher than the mass of the electron (from the approximation $\mathrm{m} \gg \mathrm{m}_e$). For electrons and positrons, this assumption no longer holds and the formula needs to be adjusted. There are several reasons why these adjustments have to be done:

- The incident and target particles have the same mass. This means that the incident particle may be deflected by the bound electron. The indistinguishability of the particles must be taken into account.
- Large energy losses per event are now possible.
- The electrons will always be relativistic at energies where nuclear interactions are the primary interaction.

The adjusted formula is given in Eq. 2.2 [4].

$$-\left\langle \frac{dE}{dx} \right\rangle = 2\pi N_0 r_e^2 m_e c^2 z^2 \frac{Z}{A} \frac{1}{\beta^2} \left[\ln \left(\frac{\tau^2(\tau+2)}{2\left(\frac{I}{m_e c^2}\right)^2} \right) + F(\tau) - \delta(\beta\gamma) - \frac{2C}{Z} \right] \quad (2.2)$$

where

- $\tau = \frac{T_e}{m_e c^2}$ the kinetic energy
- $F(\tau) = 1 - \beta^2 + \frac{\frac{\tau^2}{8} - (2\tau+1)\ln 2}{(\tau+1)^2}$ for e^-
- $F(\tau) = 2\ln 2 - \frac{\beta^2}{12}\left(23 + \frac{14}{\tau+2} + \frac{10}{(\tau+2)^2} + \frac{4}{(\tau+2)^3}\right)$ for e^+

The energy loss for electrons and positrons has to be treated differently, because the maximum energy transfer is different. For an electron colliding with an electron the maximum transfer is $\frac{1}{2}\mathrm{E}_{kin}$, whilst for a positron colliding with an electron the maximum transfer is $1\mathrm{E}_{kin}$. This means that positrons and electrons will have slightly different stopping powers.

Bremstrahlung

One of the special features of electrons (and positrons) is that these particles can also lose a large fraction of their energy through radiation. A charged particle passing by a nucleus experiences the Coulomb force and is deflected. This process is called Coulomb scattering (Fig. 2.4(a)). The deflection accelerates (or decelerates) the passing particle. From this acceleration, radiation is produced. In the case of charged particles scattered in the Coulomb field of nuclei, this is called Bremsstrahlung (Fig. 2.4(b)).

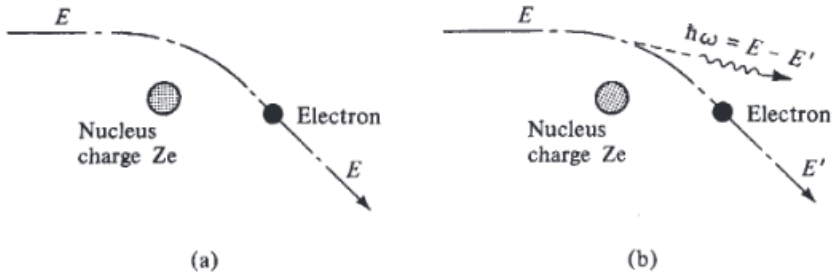

Figure 2.4: (a) Elastic scattering (Columb scattering) (b) The accelerated electron radiates a photon (Bremsstrahlung). From [5].

Bremsstrahlung is an important energy-loss mechanism for electrons and positrons, but it is very small for heavier particles (such as muons, pions and protons), at current achievable energies. Due to the emission of photons, the energy of the electrons decreases. The distance over which its energy is reduced by a factor e is called the radiation length (X_0). For electron energies $E \gg E_c$ the radiative energy loss is approximated by $-\left\langle \frac{dE}{dx} \right\rangle_{rad} \approx \frac{E}{X_0}$ [5].

Other radiation

When a charged particle passes through a dielectric medium at a speed greater than that of the phase velocity of light in that medium, Cherenkov radiation will be emitted. The emission of this radiation will lower the energy of the charged particle. However, this effect is small compared to Bremsstrahlung and it will not be discussed here.

When a charged particle passes through inhomogeneous media (such as the boundary between two different media), transition radiation will be emitted. Again, compared to Bremsstrahlung, this effect is small and it will not be discussed here.

2.2.3 Photons

The photons emitted by Bremsstrahlung can, again, have several interactions with the absorbers material. A complete treatment of these processes is rather complicated and requires the tools of quantum electrodynamics. A simplified description can be found below:

- In the photoelectric effect, the photon is absorbed by an atom, and an electron from one of the shells is ejected. This electron can have electromagnetic interactions with the material, once again.
- In the Compton effect, the photon scatters from an atomic electron and is degraded in energy. The low-energy limit of Compton scattering is called Thomson scattering.
- In pair production, the photon is converted into an electron-positron pair. This can only occur in the Coulomb field of a nucleus, which is needed to balance energy and momentum conservation, and sufficient energy is required.

At low energies (E < 10 keV), the photoelectric effect dominates, the Compton effect is small and pair production is impossible. At an energy $E > 2m_e c^2$, pair production becomes possible, and it soon dominates completely.

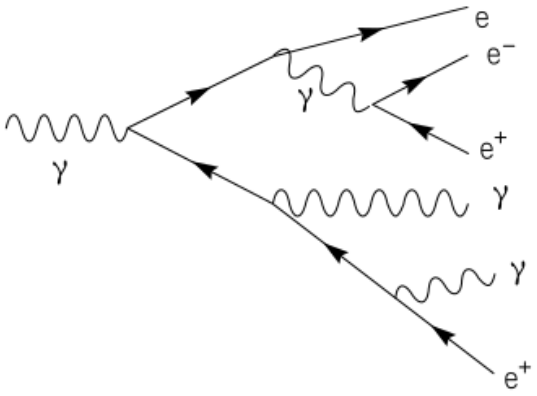

Figure 2.5: An overview of the creation of an electromagnetic shower. From [6].

When the initial photon (or electron) has enough energy to create multiple electrons, an electromagnetic shower can be produced. The initial photon can create an electron-positron pair. These two produced particles will create more photons by Bremsstrahlung, which will again create more electron-positron pairs. This process will keep repeating itself until the energy of the photons is not high enough anymore to create new pairs. At this point, the shower dies. The process of the creation of an electromagnetic shower is drawn in Fig. 2.5.

2.3 Detectors

High energy particle-accelerators produce lots of particles per collision. To fully analyze these events, one must determine what particles are created and how much energy they posses: detectors have to be made. In this chapter, some of the essential components of detectors (in special: electromagnetic calorimeters) are discussed. In Chapter 3, the specific set-up of the FoCal detector prototype will be further described.

2.3.1 Calorimeters

Calorimeters are used to measure the energy of particles. When a charged particle enters the detector, it can create a particle shower. The energy of these particles is deposited in the absorber material of the detector and the total amount of this deposited energy will be measured to identify the energy of the single incoming particle. Electromagnetic calorimeters are designed to specifically measure the energy of particles that interact through the electromagnetic interaction, as opposed to hadronic calorimeters.

A distinction can be made between sampling and homogeneous calorimeters. In a homogeneous calorimeter, the complete detector is made out of one material. This means that the signal can be measured over the entire detector. On the contrary, in a sampling calorimeter, the material that produces the shower is different from the material that measures the signal. This means that the signal can only be measured in specific locations, but it has the advantage that both the longitudinal and transverse depth (Molière radius) of the shower can be decreased by using a very dense material in between signal locations.

2.3.2 Scintillation counters

A scintillation counter is composed of two objects: a scintillator and a photo-multiplier. Scintillators are most frequently made from either sodium iodide or plastics. Plastic scintillators are cheaper than inorganic ones, but their efficiency for photons is notably lower.

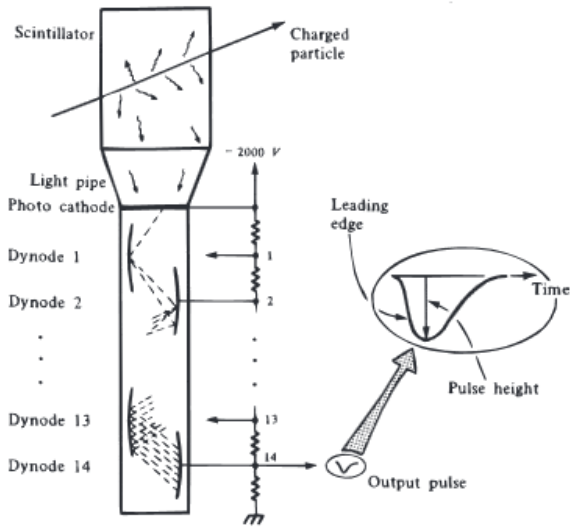

Figure 2.6: A schematic drawing of a scintillation counter. A charged particle passing through the scintillator produces photons, which travel through the light pipe into the photomultiplier. From [5].

When a charged particle passes through a scintillator, it will create excitations of the electrons in the atoms of the scintillator. De-excitation occurs when photons are emitted. The produced photons will travel through a light pipe to the photo-multiplier. This photo-multiplier is composed of a cathode, several dynodes and an anode. The photons will release electrons at the cathode, which are accelerated and focused on to the first dynode. Every time an electron hits a dynode, several new electrons are released. This happens for each dynode, until the electron beam is connected to the output-electronics. Up to 10^9 multiplying factors can be achieved. A schematic drawing of a scintillation counter is shown in Fig. 2.6.

Scintillation counters are frequently used in detector mechanics, because of their ability to detect charged particles. The voltage between the anode and the cathode has to be adjusted to get the correct detection limit of the desired particle.

2.3.3 Silicon detectors

Silicon detectors are semiconducting detectors. When a charged particle moves through the doped silicon, electron-hole pairs will be created. This gives rise to an ionization current that can be measured. One of the main advantages of these semiconducting materials is that they can be made relatively small, which is useful when you want to have a good spatial resolution. Silicon detectors have a much higher resolution than older technologies such as cloud chambers or wire chambers. Disadvantages are that silicon detectors are relativity expensive and sophisticated cooling is required to reduce the leakge currents. Additionally, the silicon detectors will degrade from radiation over time.

Chapter 3

FoCal prototype detector

In this chapter, the FoCal prototype detector setup will be described in more detail using the information from previous chapters. Some parts of the software are covered, to provide enough information for the rest of this thesis.

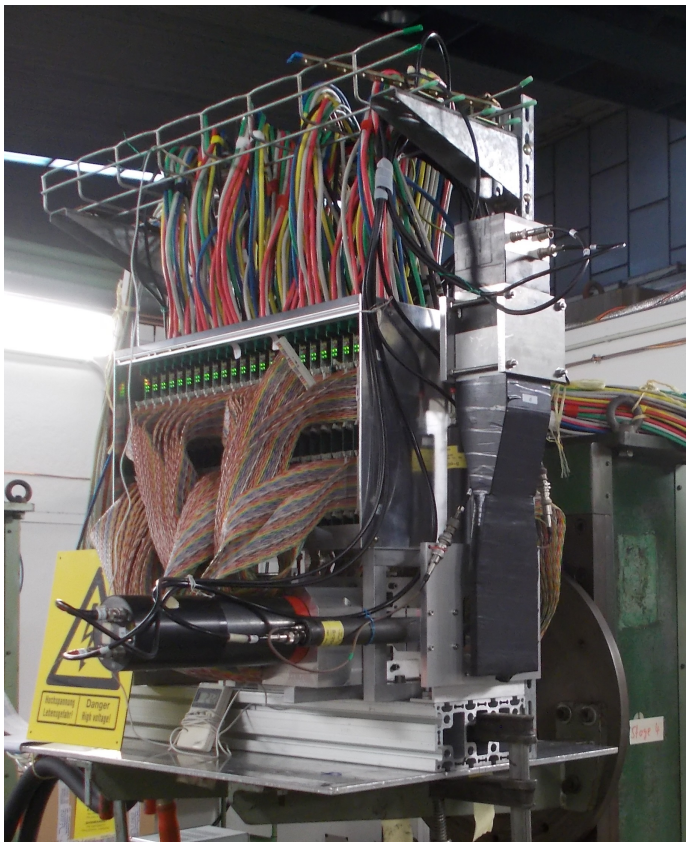

Figure 3.1: The FoCal prototype detector at DESY.

The FoCal prototype detector setup is shown in Fig. 3.1. In this picture the scintillation counters and parts of the data-acquisition system can be spotted. The individual components will be described in more detail below.

3.1 Main setup

The FoCal prototype detector is an electromagnetic digital sampling calorimeter. The main components of the detector are two scintillation counters (one in front and one in the back of the detector), 24 layers of multiple silicon detectors (sensors) and tungsten in between layers. These layers are kept at a stable temperature through a cooling system. The sensors are read out via printed circuit boards and this information is sent to the data-acquisition system, through various components.

3.1.1 Scintillation counters

The scintillation counters of the FoCal prototype setup consist of a scintillator and a photomultipliertube. The scintillator is composed of a 40 x 40 x 10 mm^3 piece of NE104 POPOP plastic (1, 4-bis-[2-(5-phenyloxazolyl)] - benzene). The two main scintillation counters are positioned in the front and in the back of the detector.

In the case of incoming electrons, the front scintillator will measure the charged particle and output a signal. The energy of this electron will be completely absorbed by the material in the detector. This means that no electrons should be exiting the detector. Thus, the back scintillation counter should not measure any particles coming from the electromagnetic shower.

It is a different situation when cosmic muons are entering the detector. Again, the front scintillation counter will detect the particle and output a signal. Opposite to electrons, cosmic muons are so massive that they will go through all layers of the detector. In this case, the back scintillation counter will also measure the muon. If the front scintillation counter and the back scintillation counter give a signal at the same time (the speed of the muon is greater than the time-resolution of the scintillation counter), we know a muon has traveled through the detector. The combination of these signals is called a *trigger*. It is possible to filter on data which has these triggers, so that the data in which nothing happens can be removed. This is useful for continuous data collection, where a lot of memory would be needed otherwise.

For the measurements at DESY, three additional scintillation counters were placed in front of the detector: the horizontal (H), vertical (V) and present (P). These scintillation counters give additional information, whilst the front (F) and back (B) scintillation counter are still measuring. Out of these 5 scintillation counters, combinations can be made. So, it is possible to, for instance, make a coincidence signal of the output of the H and V scintillation counters. This trigger would be called HV.

3.1.2 Sensors

The FoCal prototype detector uses PHASE II MIMOSA23 Monolithic Active Pixel Sensors (MAPS) chips designed by the Institute Pluridisciplinaire Hubert Curien (IPHC) as sensors. These sensors are silicon detectors. In the detector, sensors with three different thicknesses of active silicon are used; with 14 µm, 15 µm, and 20 µm silicon.

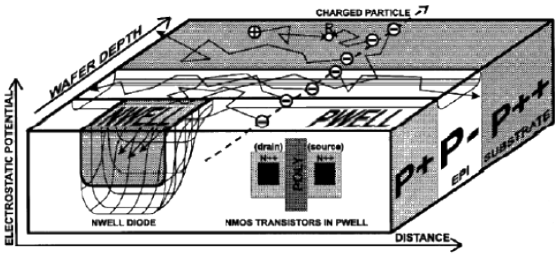

Figure 3.2: A schematic drawing of one pixel in a sensor. From [7].

The sensors have different doping levels in each layer. These different layers are the p++-layer, the p+-layer and the p-epitaxial layer. Charge is collected in a n-well. The p++ and p+ will cause the electrons to flow in the direction of the n-well. Similarly, holes flow in the opposite direction. One complete pixel of a sensor is shown in Fig. 3.2.

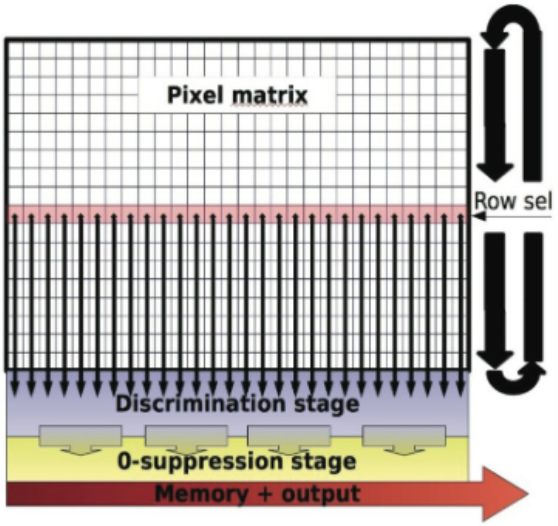

Figure 3.3: Illustration of the readout of a single sensor. From [8].

A sensor is 19.52 mm by 20.93 mm in size with an active area of 19.2 mm by 19.2 mm, containing 640 by 640 square pixels of a 30 µm pitch. The 640 lines are grouped into four *channels*, each of 160 lines. The sensor read-out is done for one line at a time. This is being controlled by a line-selection circuit in the sensor. The lines can be read out with a time of 1 µs per discriminator (thus 640 µs for the entire sensor). The read-out process is illustrated in Fig. 3.3. By selecting all the lines one by one from the first line to the last, the complete sensor is read-out. The full read-out of a sensor is called a *frame*.

It is possible for a pixel of a sensor to turn on, even when no particles are passing the detector. Some pixels have a higher tendency to fire than other pixels. Also, if a pixel is (partially) broken, it is possible for the pixel to be turned on all the time. If a pixel is active, whilst is was not triggered by a particle, we call the signal *noise*. For these effects, corrections will be made in the later analysis.

The sensitivity of the sensors can be tuned with two variables, VREF1 and VREF2. Here, the VREF1 value mainly determines the threshold of the signal of the sensors. Increasing the VREF1 value will cause less response in the sensor. The VREF2 value is mainly responsible for the uniform response on the sensor sensitivity along the row. This means that a change on the VREF2 value will change the balance in the sensor. These two settings are closely related. A change on the balance can influence the response of the sensor, and vice versa.

Previous work has been done on improvements to these values (see [10] and [11]). VREF2 was set to be as balanced as possible and for VREF1, a noise-level of 10^{-5} was chosen. This value was made uniform over all the sensors.

When cosmic muons travel trough a sensor, they will deposit energy in one pixel of a sensor. The charge that this muon generates will generally be so big that charge will diffuse into neighboring pixels. This effect is called *charge sharing*. In the current settings (noise level of 10^{-5}), a cosmic muon will activate about 2-4 pixels, every time it passes through a sensor. The average number of pixels it activates can be extracted from the data and is called the *clustersize*.

3.1.3 Layers

The detector consists of 24 layers of silicon detectors. Two sensors next to each other form one *module* and two modules are placed upside down and opposite to each other. This means that in every layer four sensors are positioned. The output of every sensor is connected to a *printed circuit board*. One module is shown in Fig. 3.4. Approximately one radiation length of tungsten is placed in between layers. Between layers 21 and 22 there is an additional 6.7 X_0 radiation length, which makes the total radiation length after the last layer approximately 28.1 X_0. Tungsten is chosen because of its very high density, which makes it useful for containing the shower.

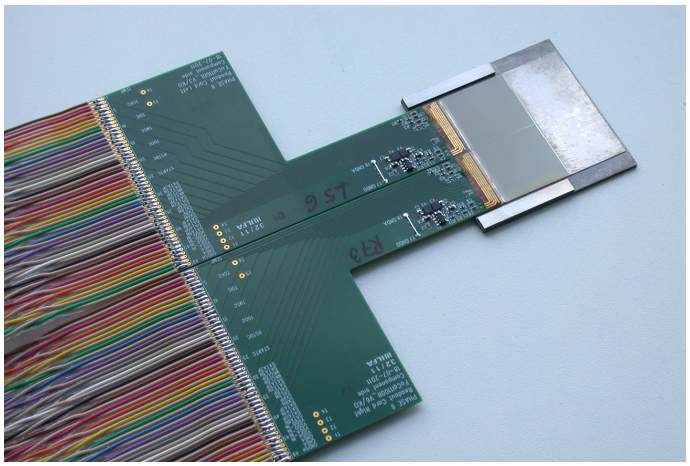

Figure 3.4: One module of the detector. Two sensors form one module and two modules form one layer. From [9].

The performance of the sensors is heavily dependant on their temperature. When the temperature of the sensors increases, their noise level will increase simultaneously. To get the most stable detector in time, the layers of the detector are cooled via a water-cooling system. The temperature of the water is set at a stable level.

3.1.4 Data acquisition

The printed circuit boards will transfer the data via network cables to two Spartan-chips (FPGA integrated circuit) and one memory-buffer. The chips and the memory-buffer are contained with the so-called *Virtex-boxes*. In this setup, two of those boxes are used. The Spartan chips regulate the timing of the read-out of the chips. This is done separately for each layer, where in each layer one sensor is chosen to distribute the clock of that particular layer.

The retrieved data is stored in the buffer, because writing speed of the disk drive of the computer is not high enough to process all data at once. The buffer will gradually be filled by the incoming data. It is full when 814 frames have been collected. This collection of 814 frames is called a *spill*. The collection of multiple spills is called a *run*.

Once the buffer is full, the data will be sent to the FoCal data-acquisition compouter and the buffer will be cleared. When this is done, another measurement can be taken. This means that there is a certain downtime in between measurements when the data is being sent, and thus the data-acquisition is not continuous. The overview of the data-acquisition system in shown in Fig. 3.5.

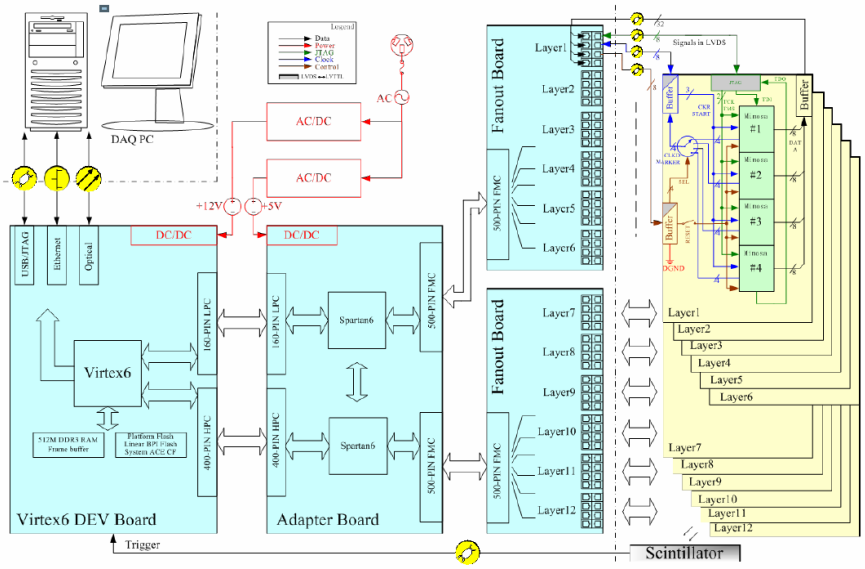

Figure 3.5: An overview of the data-acquisition from the sensors to the FoCal DAQ Compouter. The parts in blue are contained within the Virtex-box. The yellow layers are the printed-circuit boards. In this overview only one Virtex-box is shown; in the setup there are two. From [12].

When the measurements are finished, the data can be accessed on the so-called FoCal DAQ computer. This computer also stores some of the files used by the detector. For instance, one can change the VREF1 and VREF2 settings, as well as the read-out method used. There are several options for the read-out method, but the two most used are cosmic mode and beam mode:

- In cosmic mode, data will only be collected if the scintillation counter in the front and the scintillation counter in the back give a signal at the same time (so that they have a trigger). This mode is primarily used for the detection of cosmic muons.
- In beam mode, the detector will collect all the frames of the sensors and no selection is made. This means the data will also contain frames in which nothing happened. It is possible to later filter these frames out.

3.1.5 Electronic components

There are several important electronic components required in the FoCal prototype detector. A small description on some of the components is given below:

- A discriminator unit provides the transformation from analog to digital signals. This unit is used for the digitalization of the signals of the scintillation counters.
- Scalers are used to measure counts in a certain time interval. This unit is useful to measure the intensity of an incoming particle beam.
- The coincidence unit is used to combine the logic signal of two scintillation counters. This device can provide both AND and OR outputs. The combination of these elements can be used to create any electronics system desirable. The coincidence unit is used to create the triggers on which the detector collects data.
- The delay unit allows a delay of a few nanoseconds in the trigger systems. This is to make sure that small timing differences (for instance, because of different cable lengths) do not disturb the output signals.

3.2 Current software

The data that comes out of the buffer cannot be used immediately: several steps have to be taken first. The first step in this process is the *demultiplexing* of the data. Demultiplexing is a data formatting process. This needs to be done for all data, for all the measurement modes. This chapter will elaborate more on the remaining steps.

3.2.1 Synchronization

Every time a frame is read out correctly, the channels in a sensor will output a *synchronization* signal. Since the maximum capacity of the buffer is 814 frames, the maximum number of synchronizations per spill is also 814. If the synchronization is less than 814, it means that the channel is acting unstable in time.

3.2.2 Pedestal

The next step in the data analysis is to create a *pedestal*. This process takes all the hits found in the frames that have no trigger and adds them together. So, this data should contain only noise hits. Normalization is done to check for each pixel what percentage of the time it was active.

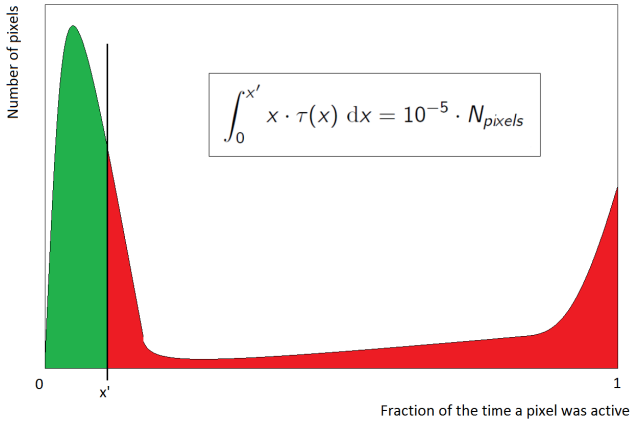

Figure 3.6: A theoretical spectrum of theoretical data. x'is the point where the cut on the data is made. The pixels in the green area will be included in further analysis, the pixels in the red area will be excluded. N_{pixels} is the number of pixels in one sensor (409600).

The data from this pedestal can be used to create a spectrum of the noise. To get rid of the pixels that are always firing or firing inconsistently, there is a cut made on this spectrum. A weighted integration is done and when the integration reaches (640 x 640) x 10^{-5}, all further pixels will be excluded from further analysis. The 10^{-5} noise level is an arbitrary level, and can be changed. To illustrate this process, a hypothetical spectrum of theoretical data is drawn in Fig. 3.6.

The problem with the always-firing pixels is that further analysis will take up way more time than useful (since calculations have to be done for every individual active pixel) and there will be a bias in the data. If there is a broken sensor, there will be instantly 640 x 640 = 409600 more hits. The problem with partially-firing pixels is that they inconsistently add data, which disturbs the statistics. This is an undesired effect and this is why the majority of these pixels are removed.

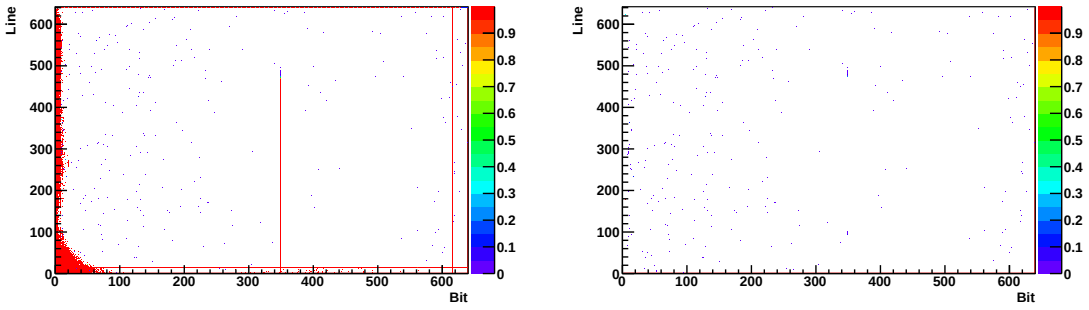

(a) The raw pedestal data

(b) The masked pedestal data

Figure 3.7: The pedestal data of DESY-run 150, Sensor: 57 is shown raw (a) and with noise removed (b). In this case, the noise in the corner is due to a mechanical defect. The color of the pixels is proportional to the noise (where 1 is the maximum). In (b) the cut on the spectrum has been made and thus the always firing pixels are removed. The data from (b) will be used for further analysis.

In Fig. 3.7, the hit-pattern from a run is shown for one sensor. The color of the pixel indicates the amount of time it was active. The blue points were active only in few frames, while the red points were active in almost all frames. The effect of the removal of the noise is evident: all the always firing (red) pixels have been removed.

3.2.3 Processing

The analysis continues with the *processing* of the data. This process uses the pedestal- and demultiplexed-data to calculate a variety of things:

- The information from the trigger is coupled to the data, so that selections are possible. This means that every frame will get a label. A frame is either *triggered* or *triggerless*, where triggerless means that no scintillation counter gave a signal during that measurement.
- The processing also includes the so-called *past-future-protection*. This is a check made to guarantee there is no overlap between single events. Only the triggered frames that have an untriggered frame in front and an untriggered frame behind the current frame will be used in the further analysis.
- The number of hits in every frame is calculated. Additionally, the positions of the hits is stored.

3.2.4 Tracks

For the cosmic muon data, it is possible to find the *track* of the particle. Dedicated software finds these tracks by looking at the group of hits in the first and in the last layer, creating an hypothetical line connecting them and checking if a certain number of pixels on the expected location were firing. If all conditions are fulfilled, a track is associated to that signal. An estimate of the clustersize in each sensor is consequently provided.

Chapter 4

Measurements

This chapter is on the measurements taken during this research: data on both a positron test beam and cosmic muons has been taken. The data from these measurements will be used for analysis later in this thesis.

4.1 Beam test

The majority of the data has been collected at Deutsches Elektronen-Synchroton (DESY) in Hamburg, Germany. This section will elaborate on the preparations for the data collection, the generation of the test beam and the measurements that have been made.

4.1.1 Preparation for beam test

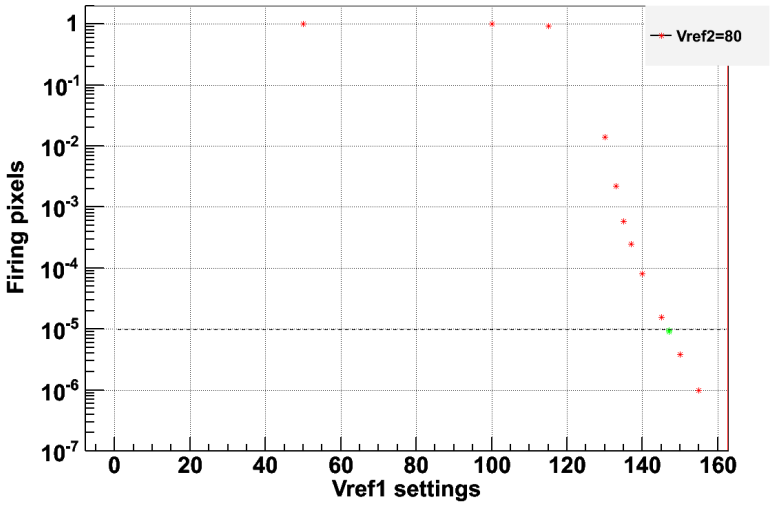

Figure 4.1: VREF1 scan for Sensor: 2. The dotted horizontal line is the 10^{-5} noise-level. From [11].

Earlier work has been done on the noise dependence on the threshold values (by tuning the VREF1 and VREF2 values) [11]. It was chosen that the following threshold settings would be measured: high (noise level of 5 x 10^{-6}), normal (10^{-5}) and low (2 x 10^{-5}). The associated VREF1 were found from scans that were already available; VREF2 remained unchanged. An example of such a scan is shown in Fig. 4.1. The settings for every threshold setting can be found in Appendix C.

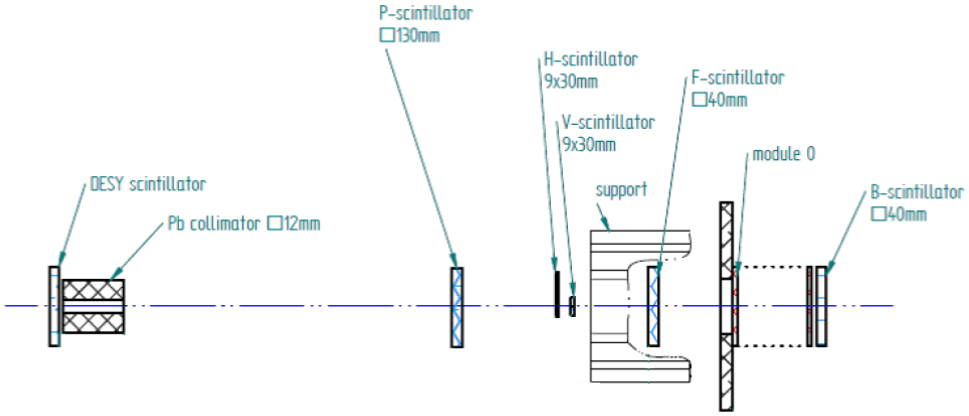

Figure 4.2: An overview of the set-up used for the test beam at DESY. From [13].

A Pb collimeter is used to center the beam to a square of approximately 1cm x 1cm and create a straight beam. The intensity of the beam was controlled by adjusting the slits on the exit of the beam. A complete overview of the set-up used is shown in Fig. 4.2.

For every scintillation counter the optimal voltage was determined. This is the voltage at which the counting speed stays almost the same at a change of voltage. This is called the plateau region. The raw data can be found in Appendix D and the associated graphs in Fig. 4.3 - 4.7.

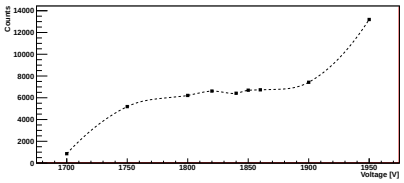

Figure 4.3: HVP counts of the present scintillation counter, as a function of voltage

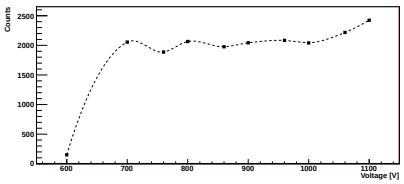

Figure 4.4: HVP counts of the horizontal scintillation counter, as a function of voltage

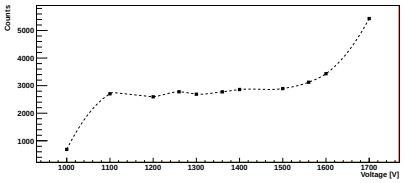

Figure 4.5: HVP counts of the vertical scintillation counter, as a function of voltage

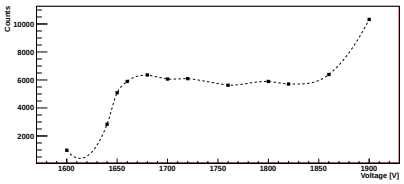

Figure 4.6: HVP counts of the front scintillation counter, as a function of voltage

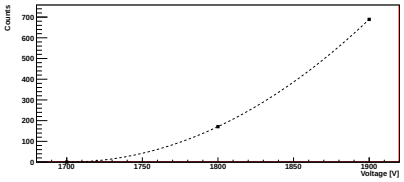

Figure 4.7: HVP counts of the back scintillation counter, as a function of voltage

The detector was put on a translation stage and aligned to the center of the beam using the HVP trigger. The trigger combinations that have been measured during the DESY measurements are:

1. HP
2. BP (for DESY-runs 1-101) / F (for DESY-runs 102-170)
3. FP
4. HVP

4.1.2 DESY II

The test beam is generated by the DESY II accelerator. Electrons / positrons are injected into DESY II and are further accelerated. Then, a Bremsstrahlung beam is generated by a carbon fiber in the circulating beam. These photons will travel to a converter (a metal plate). The interaction with this converter will, again, create electrons and positrons. Using a dipole magnet, the beam is spread out in a horizontal fan. The final beam is cut out of this fan with a collimator. This process is shown in Fig. 4.8.

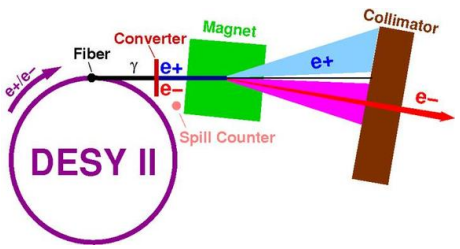

Figure 4.8: The generation of the electron/positron test beam. From [14].

By adjusting the current of the magnet, either electrons or positrons can be selected. The energy of the particles can be selected between approximately 1 and 6 GeV. However, the number of particles in the beam line decreases with the energy selected.

4.1.3 Data collection

Test beam 22 from the DESY II accelerator in building 27 was used for data collection. An overview of this building and the test beam lines is shown in Fig. 4.9.

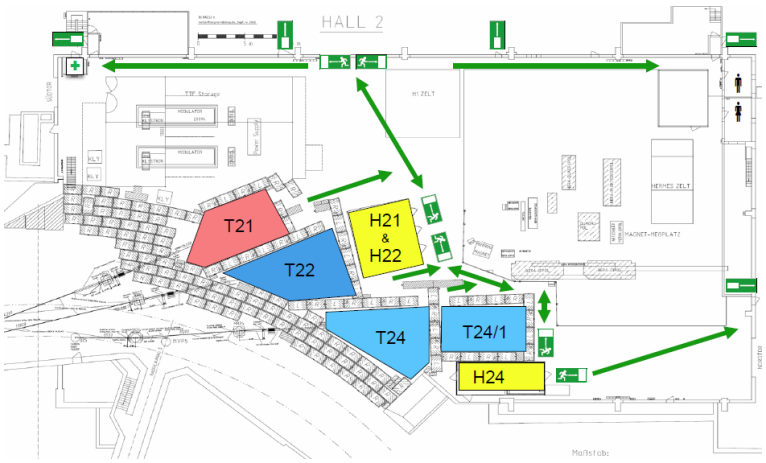

Figure 4.9: The overview of building 27 at DESY, Hamburg. Measurements were done in T22. From [14].

Since we were parasitic users, the majority of measurements were made during the night. For 7 consecutive nights data was taken. The aim was to have about 1 hour one of data in one run and two runs taken successively. After these two runs, the beam was turned off and a run of 10 minutes with no beam was taken. After this run, the beam was switched on again and the process was repeated.

Table 4.1: A summary on the data collected at DESY

Energy (GeV)	Threshold	Sets of different counting speed	Total spills
2.0	Normal	2	63+172=235
2.0	Low	1	164
2.0	High	2	45+116=161
3.0	Normal	1	225
4.0	Normal	2	177+103=280
5.0	Old settings	1	116
5.4	Normal	3	211+189+174=574

Data was taken using the beam mode read-out setting. For every different energy, about 10 hours of data taking has been done. This should be enough to achieve reasonable statistics. A summary of the collected data is shown in Tab. 4.1. A complete overview can be found in Appendix A.

The most data has been collected on 5.4 GeV. This is the reason why we will use this data most frequently throughout this thesis. For 2.0 GeV, data with three threshold settings has been collected. This data will be used to determine which threshold setting has the best energy resolution and what the best set-up for the detector will be for future tests. The 5.0 GeV data had old threshold settings loaded. Because of this, and other reasons mentioned later, these data will not be used in further analysis whatsoever.

4.2 Cosmic muons

After the beam test at DESY, the detector has been measuring cosmic muons almost continuously for two months. To achieve the best collection rate, the detector is placed perpendicular to the ground. Again, for the three different threshold levels data has been collected. A summary of this data is shown in Tab. 4.2. The complete overview can be found in Appendix B.

Table 4.2: A summary on the data collected for cosmic muons

Threshold	Total triggers
Normal	5003
Low	8309
High	11587

Data collection is ongoing, but, because of time constraints, only a certain amount will be analyzed in this thesis. The data analysed in this work is that of MUON-runs 547-609.

In Fig. 4.10, the position of the tracks for muons entering and exiting the detector is shown. It is evident that there are more muons entering the detector near the middle of the layer. This is because muons can enter the detector under an angle.

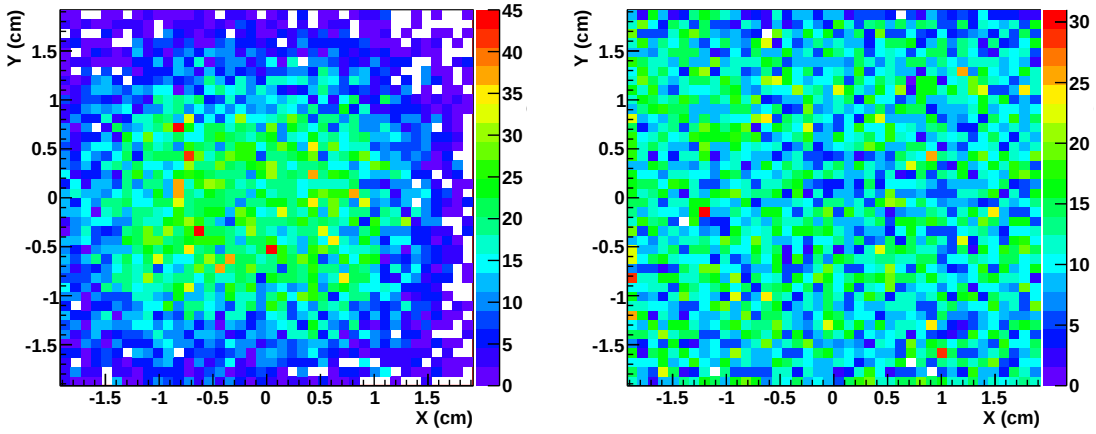

(a) **(b)**

Figure 4.10: Location of the tracks entering (a) and exiting (b) the detector. All muon data is used.

Chapter 5

Data clean-up

In this chapter, the found problems with the hardware are explained and, wherever possible, solutions are given. Some of the problems have not been solved. For those problems, suggestions for solutions are provided. The results of this chapter will be used to create a mask for the data. The influence of this mask on the data will be checked in Chapter 6.

5.1 Bad runs

Some of the runs of the measurements need to be removed from the data, because they had errors associated with them. These runs are found below.

5.1.1 Empty runs

Runs 82 and 84 of the DESY data are empty. For these runs, a data-collection was started, but not finished. In the mentioned cases, this is because the data-collection was interrupted before anything was written to the disk. These runs can simply be ignored.

5.1.2 Runs with missing data

Some of the runs seemed to have data missing. For instance, the synchronization data is not created for runs 81, 93 and 121 of the DESY data. Looking at the files created, these runs seem to have all data necessary to function for all scripts. It is unclear where this problem comes from and more investigation has to be done. For the rest of the analysis, these runs are not used.

5.1.3 Different threshold settings

The 5.0 GeV measurements (DESY-runs 1-29) had the old threshold settings loaded. Different threshold settings mean that each sensor has a different response to the incoming beam. This means that no comparison between runs of different energy can be made. These runs will be not be used in the rest of this thesis.

5.1.4 Synchronization errors

Strangely, the synchronization of the Virtex-box 0 was different from Virtex-box 1 in some DESY-runs between 1 and 19. This is also found for Virtex-box 1 in DESY-run 119. The number of synchronizations per spill is shown in Fig. 5.1. Here, the vertical bars (different values between Virtex-box 0 and Virtex-box 1) indicate that more data was written for Virtex-box 1 than for Virtex-box 0. It is found that the synchronization in Virtex-box 1 has 814 more synchronizations (thus an entire spill) than Virtex-box 0, for said runs.

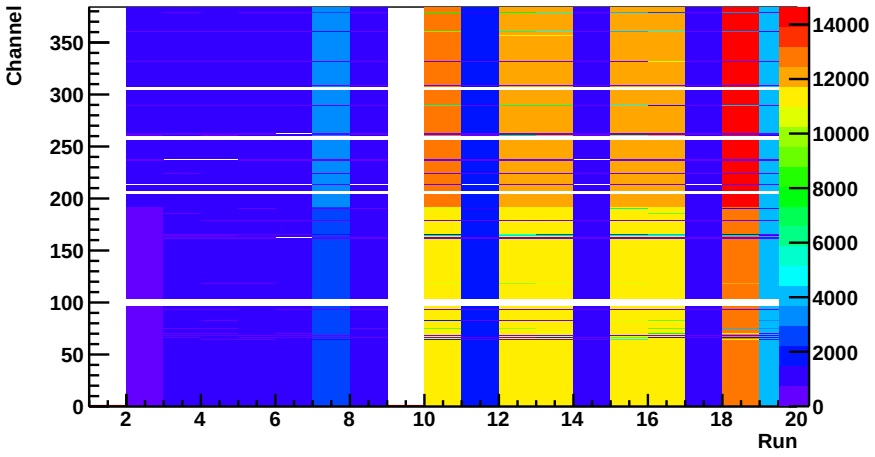

Figure 5.1: The synchronizations per channel per run for DESY-runs 1-20

For DESY-run 119, it is very likely that the data-taking was interrupted half-way through. This means that the data for Virtex-box 0 was written, but the data for Virtex-box 1 was not. Some of the functions rely on the combination of both Virtex-boxes, so this can be why the synchronization is not correct.

Above explanation does not, however, explain the errors found in DESY-runs 1-19, since the data of Virtex-box 0 is always written earlier than Virtex-box 1. More investigation has to be done on this problem. Since these runs were already not taken into account (because of the different threshold settings), we will not worry about this problem in the remaining part of this thesis.

5.1.5 Beam input

The beginning of the data-taking of a beam of different energy involved adjustments to the intensity and energy of the beam input. When different intensities are used, the response of the detector could change due to possible signal pile-ups. It is unlikely this effect will alter the response, but it is better to be safe. These starting-up runs will not be used for further data-analysis, but, since they generally only have a few spills, not much data is lost.

5.2 Hot channels

In the untriggered frames of the runs with beam, it was found that the lines in one channel randomly turned on in a few frames. We will call these channels *hot channels*. These hot channel have not been found in the pedestal data of the no-beam runs, most likely because these have less data. An example of a hot channel is shown in Fig 5.2. The effect of a hot channel is that hits-distribution will be disturbed, and thus the energy resolution of the data will be decreased.

Some of the hot channels that were found are:

- Sensor: 32 in DESY-run 135
- Sensor: 40 in DESY-runs 47, 52, 110, 112, 167 and 168
- Sensor: 43 in DESY-runs 52, 112, 124, 126, 135, 140 and 167
- Sensor: 56 in DESY-run 132

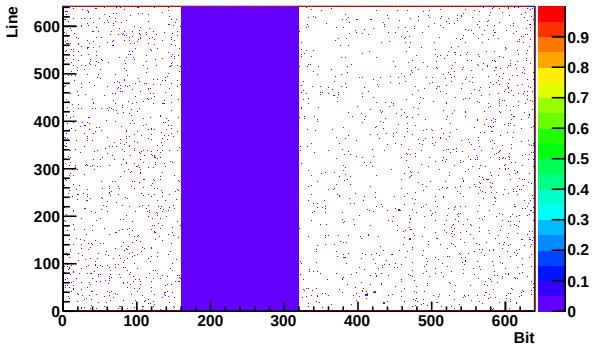

Figure 5.2: An example of a channel that is completely turned on for a few frames (also: hot channel) that is found in the pedestal data of DESY-run 132, Sensor: 32

No proper solution for this problem has been found yet. It would be possible to include a frame-quality check, since a frame will instantly have at least $160 \times 640 = 102400$ pixels more. For instance, every frame that has more than 50 000 hits could be excluded (the threshold should be lower than the actual value to compensate for possible masking). This is done in Tab. 5.1, to investigate this possibility.

Table 5.1: An investigation on the number of times hot channels are active in the data

Run	Total frames	Frames with $\geq$ 50 000 hits	Percentage [%]
52	31639	2	6.3×10^{-3}
112	19384	788	4.1
124	18684	805	4.3
126	17875	803	4.5
135	12997	806	6.2
140	17019	783	4.6
167	17045	794	4.7
168	10556	1	9.5×10^{-3}

No relation between the occurrence of hot channels has been found. It is worth noting that some of the hot channels occur in the same runs (e.g. DESY-run 135 and 167). However, this could be just coincidence.

5.3 Hot lines

Series of activated pixels (henceforth: *hot lines*) were found to turn on randomly. The rate at which this happens was different for every line. When these lines turn on, they will have anywhere from 1 to 640 extra active pixels. These pixels are not masked by the pedestal file, since they occur very rarely. This effect causes some of the analysis-functions to malfunction and the hit-distributions is biased. Hence, they should be removed from the data.

Table 5.2: An investigation on the number of times hot lines are active in the data

Hot line	Percentage [%]
Sensor: 38	0.01
Sensor: 43	0.06
Sensor: 84	0.13

It was investigated what percentage of the time some of the hot lines were active. These results are shown in Tab. 5.2.

The number of pixels firing in the smallest hot line is approximately 100 pixels. To remove the hot lines, the noise above the threshold level of 10^{-5} is removed from the data, as before. Now, the mask is created so that every line with > 100 pixels active (where active means it has turned on at least once) will be masked. This procedure is shown in a single run for a single sensor in Fig. 5.3.

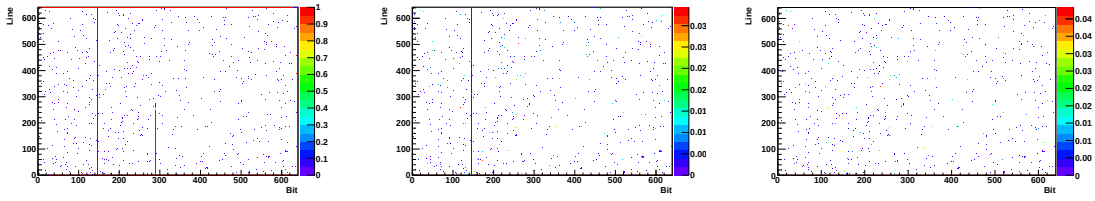

(a) Raw data **(b)** Masked on the noise **(c)** Hot line removed

Figure 5.3: Two hot lines found in the pedestal data of DESY-run 157, Sensor: 84. (a) The hot line on the right will be masked by the normal removal of the noise. (b) This does, however, not remove the left hot line, since it was only active in a few frames. This is done by masking all lines which have > 100 pixels active. (c)

The way we used to detect the hot lines is not completely correct. When more and more pedestal files are added together, the number of pixels that have been active at least once will keep increasing. It then becomes possible for a line to have more than 100 pixels active, whilst those are all properly functioning pixels. This is a saturation effect.

To counteract above problem, it has also been looked at using sum of the noise values of each line as a detection method. It, however, was not possible to detect the hot lines from this data, because the extra noise in each pixel was very small (this is again because the hot lines occur very infrequent). The data collected at DESY is still good enough to detect the hot lines, so, for now, the detection method serves its purpose.

A further remark is that, when a hot channel is found, all the pixels in this channel are turned on for a few frames. This also means that the software will mark all lines as hot lines (and thus will be excluded). This again calls for a better way to detect hot lines. Luckily, in the frames of the no-beam runs, no hot channels were found. Hence, in the rest of the analysis the method with active pixels was used.

5.4 Malfunction sensors

Some of the sensors seems to be malfunctioning. These sensors are masked in the data to make sure they do not add any inconsistent data. Two examples of bad sensors are shown in Fig. 5.4.

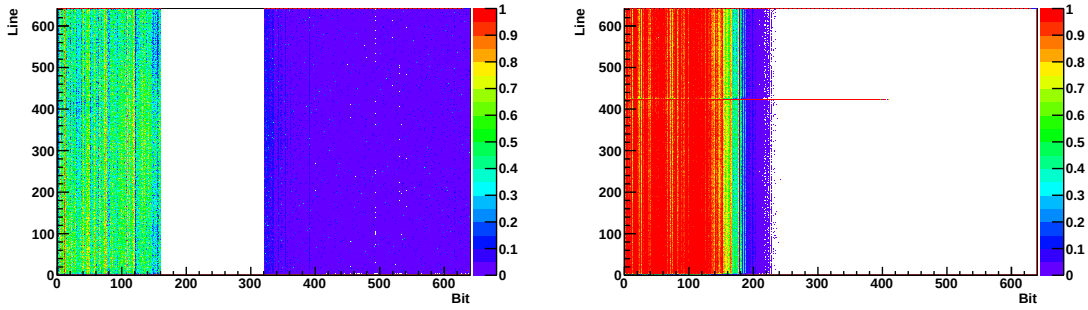

(a) Sensor: 77 **(b)** Sensor: 85

Figure 5.4: Chips that seem to be malfunctioning

All sensors that are masked because of malfunctioning are:

- Sensor: 17
- Sensor: 27
- Sensor: 33
- Sensor: 77
- Sensor: 85

It is unclear in what way these sensors affect the data. Nevertheless, their response looks bad and hence they are added to the mask.

5.5 Hot triangle

In a few sensors, there is a mechanical defect in one of the corners of the sensor. In most cases, the defect gives rise to always firing pixels, which are removed by the noise-selection. However, it was found that in some runs, these corners were found in the same shape, only shifted slightly in position. These *hot triangles* are only found in a few frames; just like the hot channels and hot lines. Because of the shape of this defect (it is not a straight line), these bad spots will not be masked by the noise threshold or the hot line selections.

An investigation on the number of times these hot triangles occurred is shown in Tab. 5.3.

Table 5.3: An investigation on the occurrence of hot triangles in Sensor: 38

Hot triangle	Percentage [%]
Between Bits 40 and 60	0.015
Between Bits 75 and 100	0.034
Between Bits 115 and 140	0.127
Between Bits 158 and 159	0.004

The hot triangle effect is only found in Sensors: 38 and 46. To get rid of these bad spots, we look at the bad spots by hand and check what needs to be masked. The entire process of masking for these sensors is shown in Fig. 5.5.

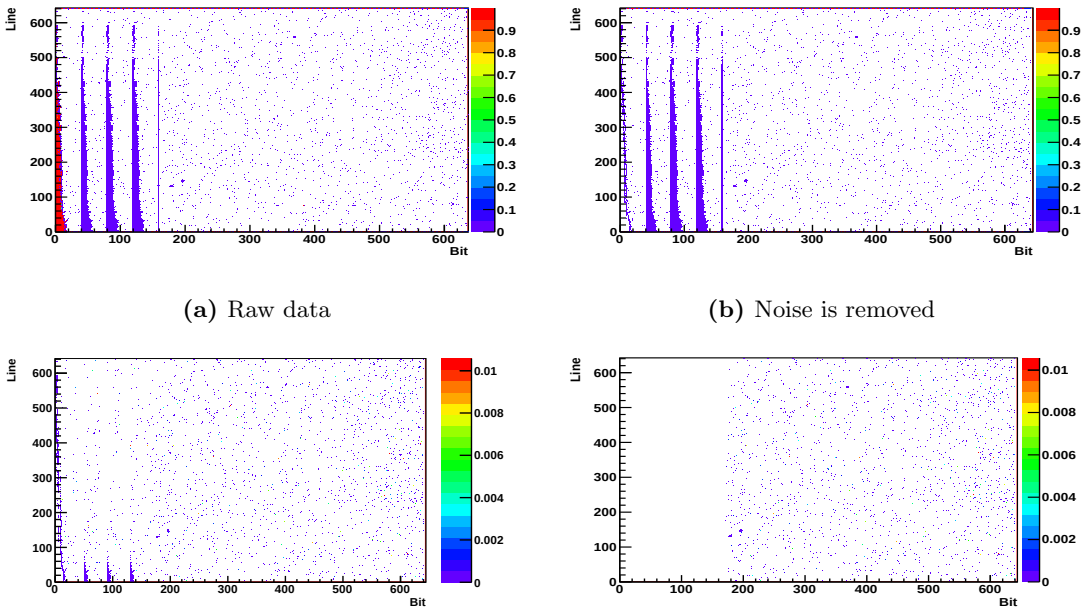

(a) Raw data

(b) Noise is removed

(c) Hot lines are removed

(d) Manual mask is added

Figure 5.5: The process of masking the pedestal data of all no-beam runs in Sensor: 38.

It, again, might be the case more data is being thrown away than necessary. For safety, we still remove the bad stuff from the sensors. The manual removal of data is applied to the following locations:

- Sensor: 38 Bit: 0-170 Line: 0-641
- Sensor: 46 Bit: 0-200 Line: 0-20

The hot triangles all seem to have the same shape (see. Fig. 5.5(a)). This makes it very likely they all have the seem origin: the corner of the sensor. Because of the fact that the hot triangle moves in position, there could be a problem with the read-out of the sensor.

The changing of the position of hits is only found in the sensors stated above, since a specific shape is needed to be able to detect this effect. It could be happening in other sensors as well, but, currently, we are not able to check this. The effect of changing positions makes the location of the found hits unreliable, and this may cause some software-functions, such as the muon tracker, to function incorrectly.

5.6 Bad channels

As explained earlier, when a channel sends data to the printed circuit board, it will give a synchronization signal. For every channel, the synchronization can be checked to see if the channel sends data consistently. The average number of synchronizations per spill is shown for all channels and all DESY-runs in Fig. 5.6.

In Fig. 5.7, the synchronization for DESY-runs 29-170 is added together for each channel. In this graph it was found that a large number of channels in fact did not have a stable number of synchronizations per spill. This means that data is being sent inconsistent, which creates an unstable detector. This is undesired and this effect should be removed.

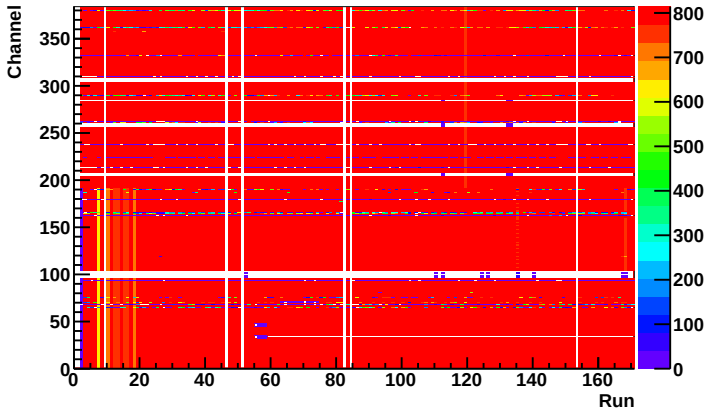

Figure 5.6: The average number of synchronizations per spill for all DESY runs. The channel number is linear with the sensor number (so channels 0-3 belong to Sensor: 0, etc.).

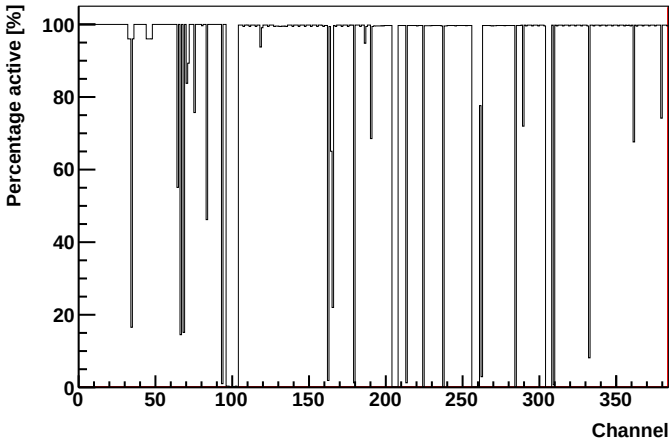

Figure 5.7: The addition of the synchronization for DESY-runs 29-171 for each channel. A normalization has been done. Channels with a synchronization of < 100 % of the total synchronizations are considered to be unstable.

The inconsistency in the detector can be solved by either masking the channel for all runs, or excluding some runs from the data. There is a maximum value to be found whilst tuning these values. We start of by stating that we value every hit equally. We then make an algorithm that calculates the maximum number of hits:

Number of hits = Hits of all channels of all runs - hits of masked channels of unmasked runs - hits of unmasked channels of masked runs

There are two parameters in this equation: one to set the number of channels masked and one to set the number of runs removed from the data. We run over these values and find the best values for the maximum number of hits.

The removal of data will decrease the statistics. However, it still remains best to get the most stable detector possible. The final values found are that all channels that have synchronization <98.9 % should be masked and, additionally, DESY-runs 81, 93, and 121 should be excluded from the data.

5.7 Pedestal data beam-runs

The frames without any triggers associated should be usable to get a pedestal of the data. However, when this is done, it was found that the supposedly triggerless frames in fact had signs of beam in their data. This beam-signal becomes more evident when multiple pedestals are added together, as is shown in Fig. 5.8.

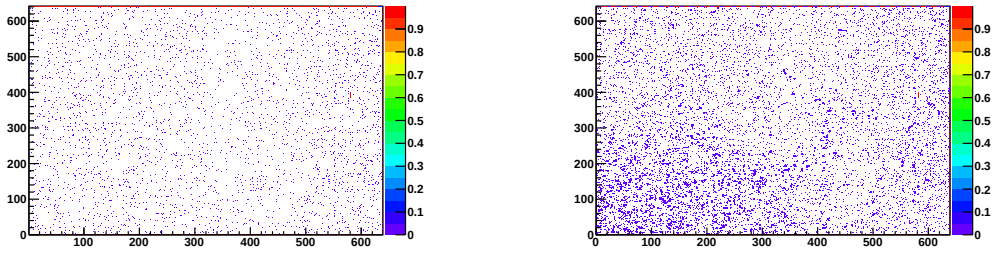

(a) Triggerless frames of the no-beam runs

(b) Triggerless frames of the 5.4 GeV runs

Figure 5.8: The comparison between the pedestal data of (a) the triggerless frames of the no-beam runs and (b) the triggerless frames of the 5.4 GeV runs of Sensor: 54. It is easily seen that the data in (b) is composed of something more than only noise. A quadrant of an electromagnetic shower can be spotted in the bottom-left corner.

To investigate what percentage of the frames in the data had beam in them (whilst the scintillation counters did not have a signal) the amount of noise in the frames was calculated. A Gaussian function was fitted to this data, to get the average amount of noise. This distribution is shown in Fig. 5.9.

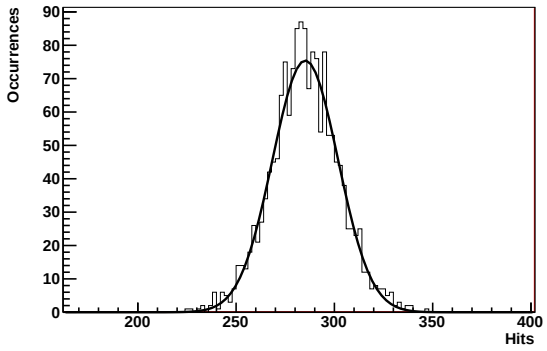

Figure 5.9: The hits in all triggerless frames of DESY-run 31. The data can be fitted with a Gaussian, which gives the mean value: 285.2 ± 0.4 and a sigma of 16.7 ± 0.3

A cut in the number of hits per frame has been set at 600 (more than twice the amount of noise) to make sure no statistical effects are responsible for hits. As frames with beam generally have more than 1000 hits, this should be enough to distinguish frames with and without beam. Only the frames with less than 50 000 hits are used, so that only frames without hot channels are looked at. Additionally, we checked for hot lines: these do not seem to be present. To summarize: if a triggerless frame has more than 600 and less than 50 000 hits, it will be counted as a frame which should have been triggered.

Above procedure takes a long time to run, so a sample of runs has been used of the 5.4 GeV data. The results are shown in Tab. 5.4.

Table 5.4: An investigation of what percentage of the triggerless frames have more hits than expected.

Run	Frames with $< 50\,000$ hits	Frames with ≥ 600 and $< 50\,000$ hits	Percentage [%]
29	13799	7	0.051
39	15425	6	0.039
123	17865	7	0.039
130	17057	8	0.047
135	12191	11	0.090
158	17855	5	0.028
161	18657	20	0.107
167	16251	25	0.154

If the data fits a true Gaussian function, number of hits between 600 and 50 000 cannot be explained by statistical effects, which makes the input of the beam the most likely the candidate of this effect. This means that the trigger-system was not fully efficient during the measurements. The number of triggers received was apparently less than the number of events actually happening.

To get rid of this problem, one could try to create a frame-check for each of the frames, to check if this frame really has no beam in the data. This creates other complications, though. More on this proposal can be found later in this thesis. Because of time-constraints, this effect is no further investigated.

Since no adequate solution was found in the this thesis, the triggerless frames of the beam-runs will simply not be used. All pedestal data will be from no-beam runs.

5.8 Trigger inefficiency

As explained above, the inefficiency of the trigger system could cause problems. One of these problems is that there could be an overlap of two showers in the detector, which will not be recognized. The past-future protection makes sure there is at least one frame between data, but with malfunctioning scintillation counters, this cannot work anymore and will give rise to an incorrect hit-distribution.

Another problem is that a scintillator counter can turn on, even when there is no particle passing the scintillator. This will mark a frame with no shower as one with shower, which will, again, give rise to an incorrect hit-distribution.

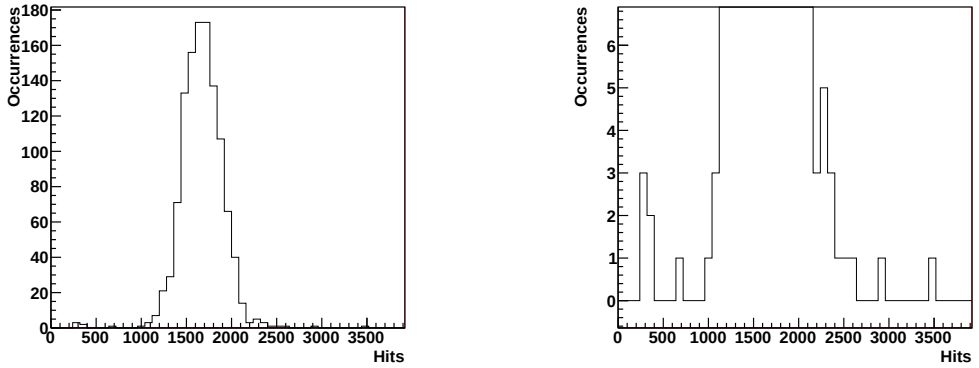

(a) Hit distribution **(b)** Detail of the hit distribution

Figure 5.10: Hit distribution of the 5.4 GeV - Set 1 data. Past future protection is active and the data is filtered to HVP triggers.

Both of these effects are found in the hit-distribution data of the 5.4 GeV - Set 1 (see Fig. 5.10). At around 300 hits, there is a peak, which matches the pedestal peak, and at 3500 hits there is a hit, which is twice the mean of the normal 5.4 GeV data. This again indicates that there might be a problem with the trigger system of the setup.

We not have a solution, since this problem is hardware related. However, from Fig. 5.10 it can be found that unexpected hits only make up approximately 0.7 % of the data. This is a small contribution and the hit-distribution will most likely not be affected by a lot. To exclude the odd events, one could make a cut in the number of hits. This is, however, very prone to errors and is not recommend to be done.

5.9 Individual masking

In the previous analysis, the mask on the data is made using just the data of an individual run. This means the masks across data will be different and a pixel can be masked in one file, but not in another. This creates an inconsistency in the detector and this effect should be removed. The inconsistency can be measured as the number of excluded pixels in each run, which is drawn in Fig. 5.11.

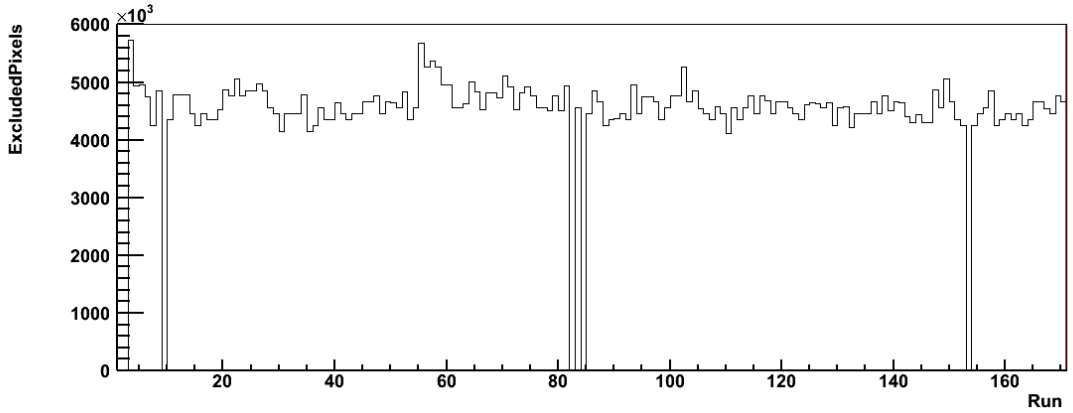

Figure 5.11: The number of excluded pixels (by the noise level) for each run, using the previous analysis. This plot shows that the data masking is different for each run, which induces an unstable detector in time.

To solve this problem, the pedestal files of all the runs with the same threshold and no beam are added together. One general mask is be made from this data.

A problem with this procedure is that the mask will keep expanding as more runs are added. This also means that if a part of a sensor is behaving badly in just one run, it will be masked in all the runs; even if it is behaving correct in the other runs. A decision has to be made whether you want more data and a variable detector, or less data and a consistent detector. We believe it is best to get the most consistent detector, so that data of all runs is equal and comparisons can be made better.

Chapter 6

Analysis of the test-beam data

In this chapter, comparisons between the masked and unmasked data will be made. A complete overview of the masking used can be found in Appendix E. Unless stated otherwise, the masked data will be used for further analysis. In Tab. 6.1, a summary of the runs that have been used for the analysis is given.

Table 6.1: A summary on the runs of DESY used for further analysis

Energy (GeV)	Threshold	Set	Runs
0.0	Normal		31, 34, 37, 40, 43, 48, 54, 59, 61, 90, 96, 99, 103, 108, 111, 114, 117, 120, 125, 128, 131, 134, 136, 137, 150, 156, 160, 163, 166, 169, 170
	Low		64, 67, 70, 73
	High		76, 79, 83, 141, 144, 147
2.0	Normal	1	50, 52, 53
		2	55, 56, 57, 58, 60, 62
	Low		63, 65, 66, 68, 69, 72, 74
	High	1	75, 77, 78, 80
		2	138, 139, 142, 143, 145, 146
3.0	Normal		106, 107, 109, 110, 112, 113, 115, 116, 118, 119
4.0	Normal	1	86, 87, 88, 89, 91, 92, 94, 95, 97, 98, 100, 101
		2	149, 151, 152, 154, 155
5.4	Normal	1	29, 30, 32, 33, 35, 36, 38, 39, 41, 42, 44, 45, 47, 49
		2	122, 123, 124, 126, 127, 129, 130, 132, 133, 135
		3	157, 158, 159, 161, 162, 164, 165, 167, 168

As previously stated, the number of hits in the detector is directly proportional to the energy of the incoming particle. One way to check the performance of detectors is to calculate the *energy resolution*. This is a quantity which states to which amount a measurement is reproducible. The formula which is applicable to this detector is:

Energy resolution $= \sqrt{\sigma^2_{\text{no-beam}} + \sigma^2_{\text{beam}}}/(X_{\text{beam}} - X_{\text{no-beam}})$

where σ is the spread and X is the mean value of the Gaussian distribution that is fitted to the hit-distribution.

One limiting factor in the energy resolution is the uncertainty in the amount of data, which goes with n^2 (where is n the number of measurements).

Another measure of the performance of the detector is the linearity. This linearity is checked by fitting a line through the mean values of the number of hits for every measured energy. The χ^2 gives an indication how linear the response of the detector is, where you want this quantity to be as low as possible.

6.1 Data selection

During the measurements, the signal of the scintillation counters has been recorded and stored with the data. One can use this information to make further selections on the data used. Normally, the HVP trigger is selected to do further analysis with.

Using above information, one can check in which frames there was an event. The past-future protection is a condition applied to the trigger stream to find frames associated with a trigger signal where no other triggers occurred (one frame before and after the frame selected). This makes sure there are no overlapping events.

In Tab. 6.2 it has been checked what the influence of the HVP selection and the past-future protection is on the data.

Table 6.2: The investigation of the influence of the HVP trigger selection and the past-future protection on the data of 5.4 GeV - Set 3. PFP = past-future protection.

Filtered on:	Events	Energy resolution
Nothing	4831	0.169
PFP	3315	0.157
HVP	1290	0.151
PFP and HVP	901	0.139

It is found that the combination of the HVP selection and past-future leaves us with the smallest number of events, but the energy resolution is the best. In the rest of this thesis the data will be filtered on the HVP trigger (Bit 4) and past-future protection will be active.

6.2 Beam and shower

The beam-position can be determined by looking at the hits of the first layers of the detector, where no shower is evident yet. In Fig. 6.1 this is done for the first three layers. The procedure used is not accurate to locate the shower position precisely, since there are effects of missing parts of sensors. However, to get a rough estimate, this procedure is sufficient.

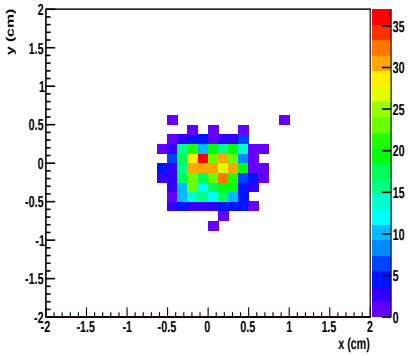

Figure 6.1: The hits in the first three layers of the data of 5.4 GeV - set 3. The beam position is found to be at: x=0.03771 , y=-0.09707.

It is found that the beam is slightly off the middle in both x and y direction, but good enough to be considered centered.

The hits in the layers are plotted to check if the layers in the detector completely capture the electromagnetic shower created by the incoming particle. These hits are shown for each layer in Fig. 6.2. It is found that the shower is well contained within the width of the layer.

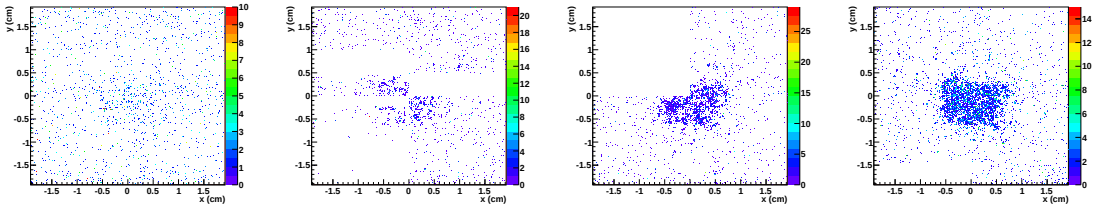

(a) Layer 0 **(b)** Layer 1 **(c)** Layer 2 **(d)** Layer 3

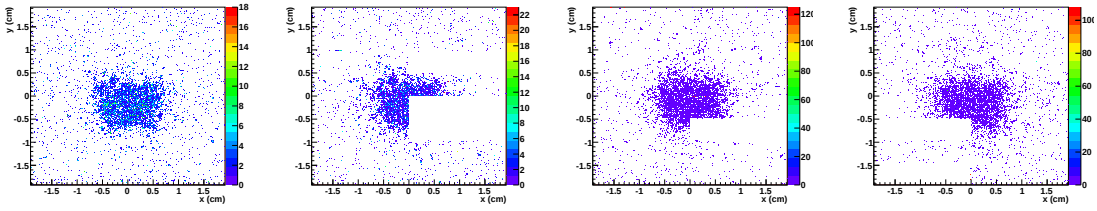

(e) Layer 4 **(f)** Layer 5 **(g)** Layer 6 **(h)** Layer 7

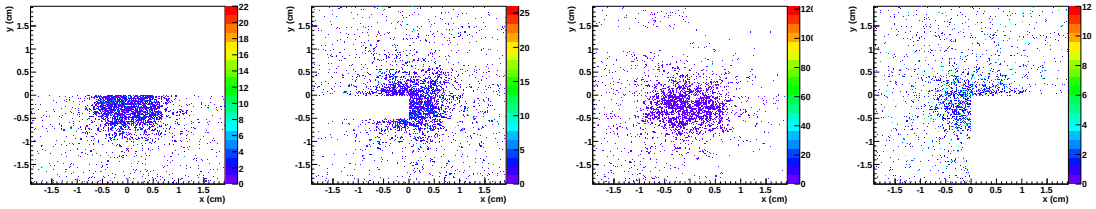

(i) Layer 8 **(j)** Layer 9 **(k)** Layer 10 **(l)** Layer 11

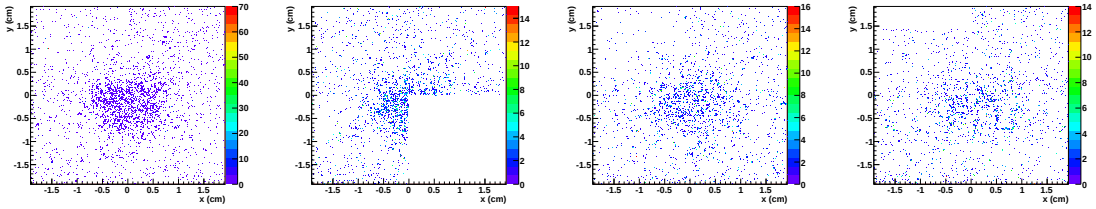

(m) Layer 12 **(n)** Layer 13 **(o)** Layer 14 **(p)** Layer 15

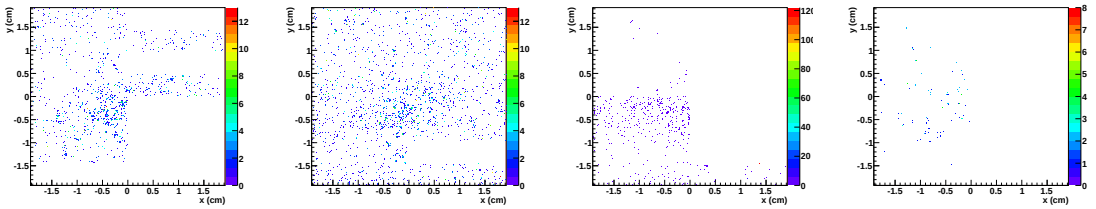

(q) Layer 16 **(r)** Layer 17 **(s)** Layer 18 **(t)** Layer 19

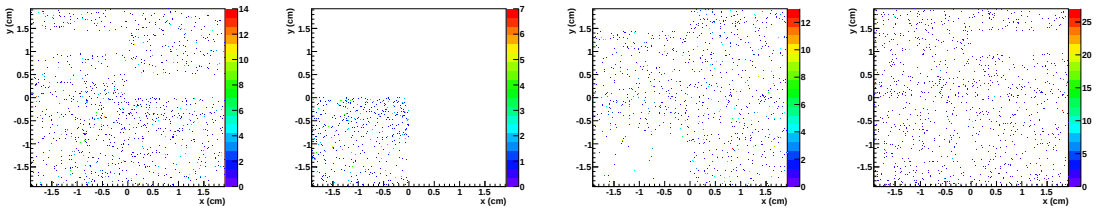

(u) Layer 20 **(v)** Layer 21 **(w)** Layer 22 **(x)** Layer 23

Figure 6.2: The hits in the layers of the detector of DESY-run 158 (5.4 GeV).

6.3 Counting speeds

The intensity of the incoming test beam can be related to the amount of HVP triggers in the data, where more triggers indicate a more intense beam. The number of showers filtered on HVP, and the number of showers filtered on HVP and surviving past-future protection can be read-out from the data files. These numbers are shown in Tab. 6.3 and plotted in Fig. 6.3.

Table 6.3: Counting speeds for the different sets of data. [1]The average number of showers that had a HVP trigger attached per spill, [2]The average number of showers that had a HVP trigger attached and survived past-future protection per spill. PFP = past-future protection.

Energy (GeV)	Threshold	Set	Average HVP per spill[1]	Average HVP + PFP per spill[2]
2.0	Normal	1	31.25	6.16
		2	63.65	13.77
	Low		64.45	14.01
	High	1	59.64	13.13
		2	39.96	8.76
3.0	Normal		42.44	10.92
4.0	Normal	1	16.97	4.43
		2	29.17	7.64
5.4	Normal	1	20.78	5.22
		2	13.96	3.84
		3	19.05	5.18

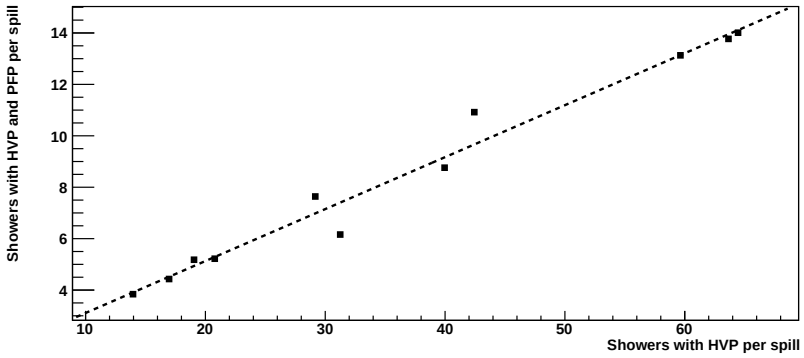

Figure 6.3: The average number of showers triggered on HVP and surviving past-future protection per spill as a function of the average number of showers triggered on HVP for the different sets of data. Fitted line: (1.09 ± 0.44) + (0.20 ± 0.01) × HVP.

It is found that the number of showers surviving past-future protection per spill increases with the number of HVP coincidences per time. Higher intensity results in higher amounts of data collected per spill. No limit on this value seems to be present in the collected points.

6.4 Effect counting speeds

Every time a new measurement was made, the slits in front of the detector were adjusted. This means that every set of data has a different counting speed, since it was hard to get the same settings as before. The counting speed should not affect the performance of the detector. Nevertheless, we will use the hit-distribution to verify if the different sets of data are indeed familiar. If this is true, we can use the sets of different energies together to achieve better statistics.

The found parameters of the Gaussian fits to the hit-distributions of the different sets of data are shown in Tab. 6.4.

Table 6.4: The mean and the sigma of the Gaussian distributions fitted to the hit-distribution of the different sets of data.

Energy (GeV)	Set	Mean hits	Sigma
2.0	1	810.0 ± 7.1	119.9 ± 6.9
	2	810.0 ± 2.7	118.0 ± 1.9
4.0	1	1317.3 ± 6.0	160.1 ± 5.6
	2	1329.6 ± 6.2	162.9 ± 5.0
5.4	1	1672.7 ± 6.1	199.4 ± 4.6
	2	1680.7 ± 7.8	200.3 ± 6.7
	3	1674.2 ± 6.8	191.8 ± 5.1

It is found that the different sets of data of 2.0 and 5.4 GeV are within uncertainty range of each other. The difference between the sets of 4.0 GeV is bigger. Nevertheless, we decide to use the different sets together and treat the different sets as one. These data will be used in the rest of this thesis.

6.5 Hit distributions

The data of all different energies is added together to get the parameters for the final hit-distribution plots. These plots, together with their parameters, are shown in Fig. 6.4.

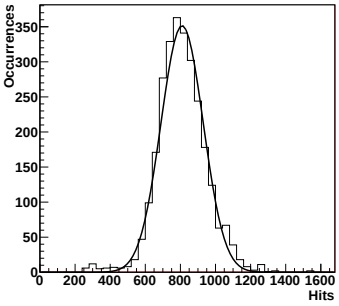

(a) 2.0 GeV: $X = 809.8 \pm 2.5$ and $\sigma = 120.2 \pm 2.0$

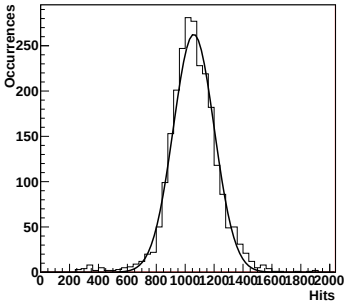

(b) 3.0 GeV: $X = 1059.2 \pm 3.0$ and $\sigma = 141.4 \pm 2.7$

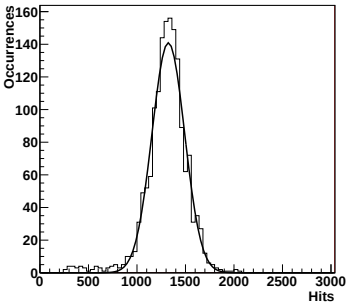

(c) 4.0 GeV: $X = 1323.3 \pm 4.4$ and $\sigma = 168.3 \pm 3.9$

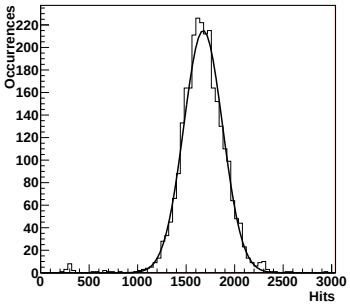

(d) 5.4 GeV: $X = 1678.9 \pm 3.9$ and $\sigma = 200.1 \pm 3.0$

Figure 6.4: Final hit-distributions

The pedestal distribution has been found earlier to be: $X = 285.2 \pm 0.4$ and $\sigma = 16.7 \pm 0.3$, for the masked data. The distributions of the unmasked data have been recorded as well, and these results are shown in Tab. 6.5, together with the new results.

Table 6.5: Comparison of the masked and unmasked data.

Energy	Mean hits		Sigma		Energy resolution	
	Unmasked	Masked	Unmasked	Masked	Unmasked	Masked
2.0 GeV	582.4 ± 2.8	524.6 ± 2.5	130.8 ± 2.2	121.4 ± 2.0	0.225 ± 0.004	0.231 ± 0.004
3.0 GeV	841.4 ± 3.3	774.0 ± 3.0	153.0 ± 3.0	142.4 ± 2.7	0.182 ± 0.003	0.184 ± 0.004
4.0 GeV	1142.7 ± 4.6	1038.1 ± 4.4	175.5 ± 3.6	169.1 ± 3.9	0.154 ± 0.003	0.163 ± 0.004
5.4 GeV	1526.8 ± 4.8	1393.7 ± 3.9	232.0 ± 4.0	200.8 ± 3.0	0.152 ± 0.003	0.144 ± 0.002

It is found that the energy resolution improved for 5.4 GeV. For 2.0 GeV, the change was slightly worse. For the 3.0 and 4.0 GeV data, the energy resolution got worse. We cannot conclude from the energy resolution whether the masking results are improvements. However, as will be shown later, the masking procedure has other benefits. It is worth noting that the energy resolution with the masked data decreased linearly, whilst with the unmasked data: 4.0 and 5.4 GeV have the same value.

6.6 Linearity

The mean hits of the different energies can be used to check the linearity of the detector. This is done in Fig. 6.5. It is found that the detector is very linear with energy, which is desired. In this plot, the hits at zero energy can be subtracted, which is done in the figure on the front page of this thesis.

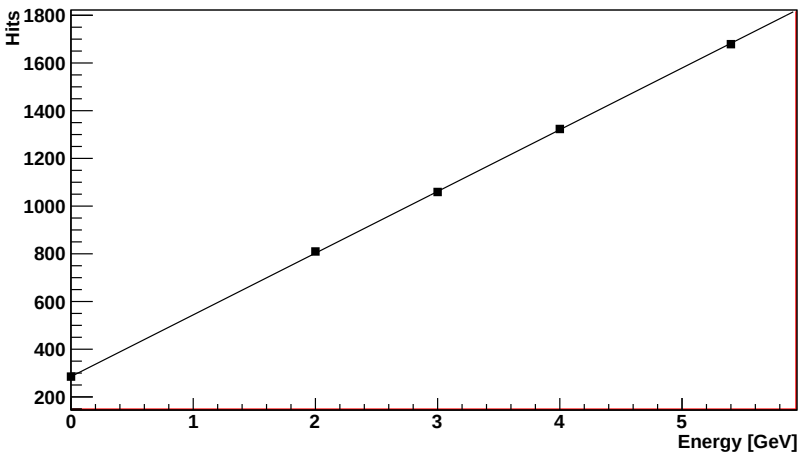

Figure 6.5: Fitted line: Hits = (285.3 ± 0.4) + (258.7 ± 0.4) × Energy. $\chi^2 = 10.5$.

The linearity of the unmasked data has been checked as well. This fitted line has an χ^2 of 43.3, which is considerably higher than the χ^2 of 10.5 of the masked data. This value is calculated without any uncertainty in the energy, so the actual numbers will be even smaller. We conclude that the masking of the data was an improvement.

6.7 Threshold settings

The threshold settings for the sensors (VREF1 and VREF2) were originally set to achieve an arbitrary noise level of 10^{-5}. To check if these are indeed good values, additional data for 2.0 GeV has been taken for noise levels of 2×10^{-5} (low threshold) and 5×10^{-6} (high threshold). To correctly analyze this data, the noise level in the software has be chosen at a different level.

The first step in the analysis is the creation of a new pedestal. The effect on the number of hits in the detector for different threshold values is shown in Fig. 6.6. In these graphs, the dependency of the number of hits in the detector on the level of masking in the software is shown.

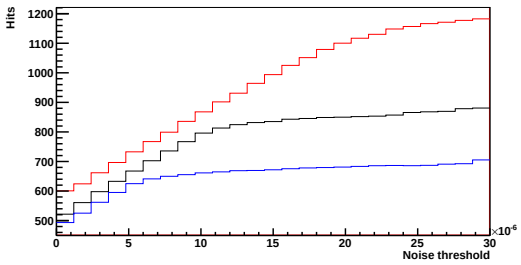

(a) Mean of the distribution of the hits for runs with beam

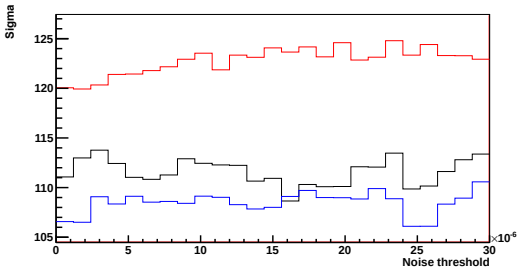

(b) Sigma of the distribution of the hits for runs with beam

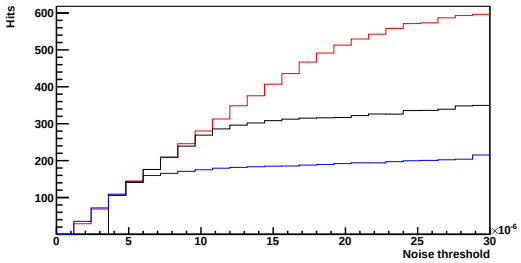

(c) Mean of the distribution of the hits for runs without beam

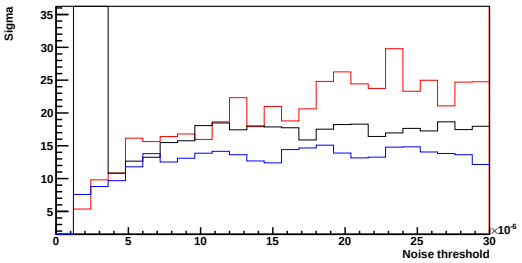

(d) Sigma of the distribution of the hits for runs without beam

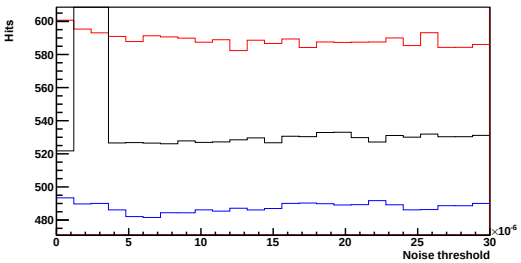

(e) Substraction of (a) and (c)

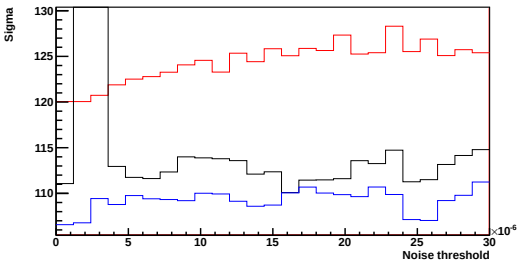

(f) Quadratic addition of (b) and (d)

Figure 6.6: Dependency of several values on the noise threshold level used by the software. The red lines have the low-threshold setting, black lines have the normal-threshold setting and blue lines have the high-threshold setting.

It is found that the number of hits in the detector (Fig. 6.6(a) and (c)) has a strong dependance on the level of masking used by the software. The distribution of the hits in the detector for the three different threshold settings is notably different. For the high-threshold setting, the curve flattens out earlier.

When the hits from the beam and from the pedestal are subtracted, the *real hits* are found (Fig. 6.6(e)). The low-threshold setting has more hits than the high-threshold setting. It is worth noting that the number of these real hits seems to be approximately constant over change of the noise-threshold level in the software.

Another interesting effect is that the sigma of the Gaussian distribution fitted to the spectrum of hits decreases slightly for lower threshold settings in the software. In Fig. 6.6(f), the quadratic addition of the sigma of the beam hits and the pedestal hits is shown. The high-threshold setting has less hits and therefore also a lower sigma.

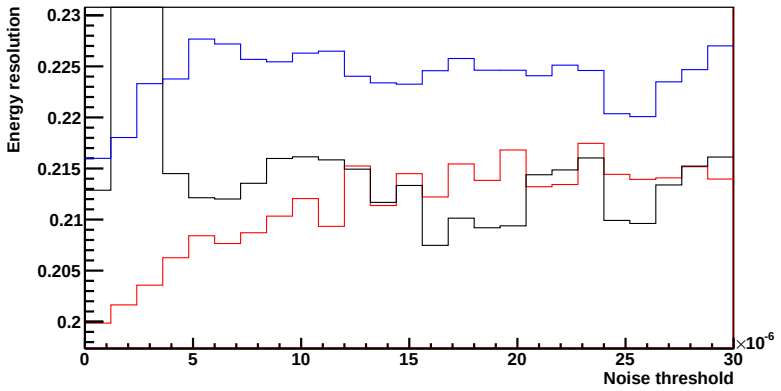

Figure 6.7: Energy resolution dependance on the noise-threshold level in the software. This quantity is found by dividing Fig. 6.6(f) by Fig. 6.6(e). The red lines have the low-threshold setting, black lines have the normal-threshold setting and blue lines have the high-threshold setting.

The energy resolution for the different threshold settings is shown in Fig. 6.7. It is found that the low-threshold setting for the sensors turns out to have the best energy resolution, especially for the low noise threshold levels in the software. It is found for all threshold settings that the lowest energy resolution can be found in the lower region of the noise-threshold level in the software. This is worth further investigation.

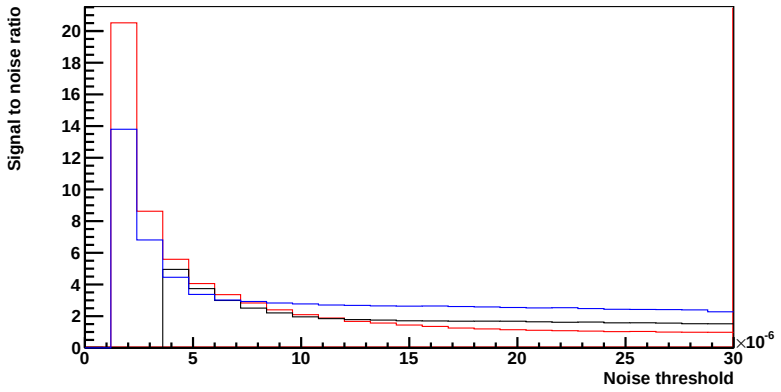

Figure 6.8: Signal to noise ratio. The red lines have the low-threshold setting, black lines have the normal-threshold setting and blue lines have the high-threshold setting.

The signal to noise ratio is drawn in Fig. 6.8. The highest ratio is found for the high-threshold setting. The ratio blows up at lower noise-threshold values, since in this region almost all noise is masked.

Using the data collected on the cosmic muons, the clustersize has been calculated for the different threshold settings. This data has only been masked on the respective noise-levels. So, the low-threshold settings (noise level of 2×10^{-5}) had a software noise masking level of 2×10^{-5}. Similarly, the high-threshold settings had a software noise masking level of 5×10^{-6}. The clustersizes, with their distributions, are shown in Fig. 6.9.

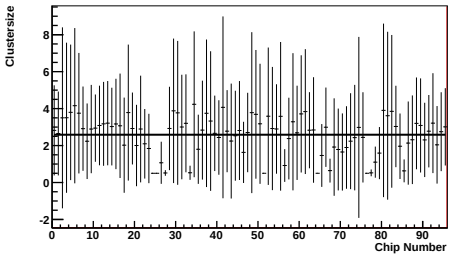

(a) Low-threshold. Line at 2.59 ± 0.10

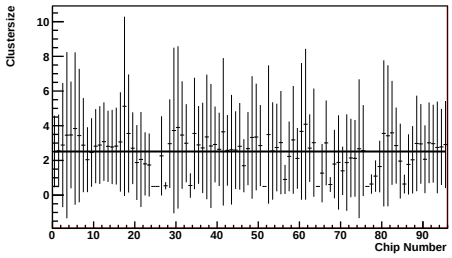

(b) Normal threshold. Line at 2.51 ± 0.10

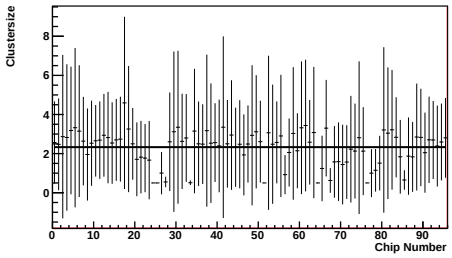

(c) High-threshold. Line at 2.33 ± 0.10

Figure 6.9: Clustersizes of the sensors at different thresholds. The dot is the median value. The uncertainties are drawn at the 25% level.

It is found that the clustersize is biggest for the low-threshold setting and smallest for the high-threshold setting. This is expected, since there are less hits found in the detector as the threshold is increased. In addition, the percentage of clusters that were not found in a sensor (or: a clustersize of 0) has been determined. The average values of the percentages are found in Tab. 6.6.

Table 6.6: An investigation on the number of times a cluster was not found.

Threshold setting	Percentage of clusters not found [%]
Low	29.9
Normal	28.0
High	29.4

No relation is observed between the percentage of clusters that were not found by the tracking software and the threshold settings.

6.8 Profile and shower shape

One of the nice features of this detector is the ability to detect particles in 24 different layers. A longitudinal profile can be made using this data. One can view the hitmaps in every different layer to get a view of the shower shape created by an incoming particle.

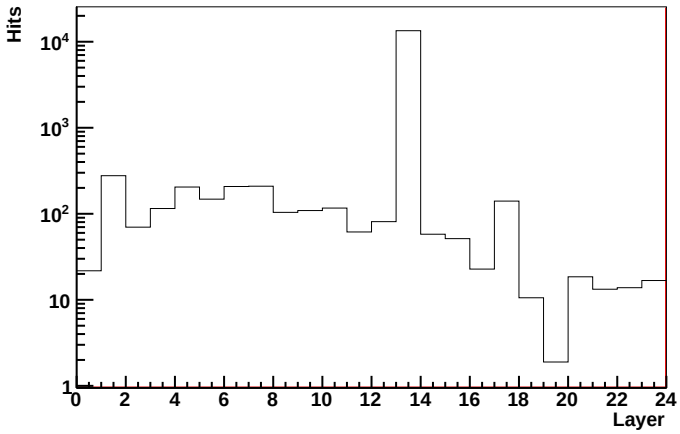

Figure 6.10: Profile of DESY-run 167. The number of hits in layer 13 is disproportional. This effect is due to hot channels in this layer.

The profile of DESY-run 167 is drawn in Fig. 6.10 to show the effect of a hot channel in the data. This run has a very high number of hits in layer 13. Since no good solution for these hot channels was found, it has been decided to exclude this run, along with DESY-runs 124, 126 and 135 (which have the same problem), from the data used in the profile.

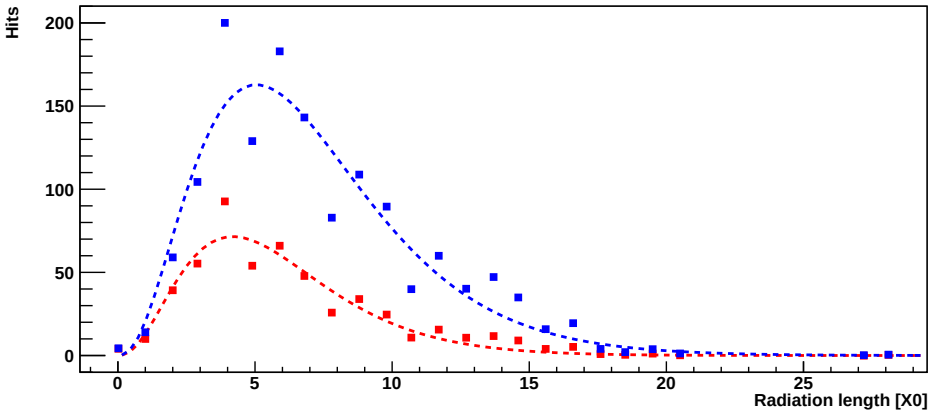

Figure 6.11: Profile of the 5.4 GeV data (blue, without DESY-runs 124, 126, 135 and 167) and the 2.0 GeV data (red). Fitted lines are gamma functions, described by Eq. 6.1. Parameters red line: $E_0 = 23.8 \pm 0.8$, $a = 2.54 \pm 0.06$, $b = 0.606 \pm 0.012$ / parameters blue line: $E_0 = 33.9 \pm 0.5$, $a = 2.54 \pm 0.02$, $b = 0.504 \pm 0.004$.

The profile of all 5.4 GeV data (except DESY-runs 124, 126, 135 and 167) and 2.0 GeV data, both with the noise subtracted, is shown in Fig. 6.11. In this graph, the layer numbers are converted to the radiation length. Beyond the first radiation length, the mean longitudinal profile of the energy deposition is well described by a gamma function [15]. The data will be fitted to Eq. 6.1, with E_0, a and b free parameters.

$$\frac{dE}{dt} = E_0 t^a e^{-bt} \tag{6.1}$$

It is evident that the 5.4 GeV data has more hits per layers. In addition, the peak of the shower seems to be shifted slightly further in the detector. The formula for the associated shower maximum is given in Eq. 6.2.

$$t_{max} = \frac{a}{b} \tag{6.2}$$

It is found that the peak locations for 2.0 and 5.4 GeV are, respectively, 4.19 ± 0.13 and 5.04 ± 0.06. From theory, we have a second definition of the shower maximum, given in Eq. 6.3.

$$t_{max} = k \ln \frac{E_0}{E_c} \tag{6.3}$$

Eq. 6.3 expects that the change in peak position is $\ln 5.4 - \ln 2.0 = 0.99$. Our fits give a peak change of $5.04 \pm 0.06 - 4.19 \pm 0.13 = 0.85 \pm 0.14$. Found values agree within the uncertainty range.

The jumps in the profile are caused by sensors that are either masked, or not functioning. The number of useable pixels in each layer is therefore different. Nevertheless, the distributions seem to fit the data nicely.

Chapter 7

Conclusions

This research started with the collection of test beam data at DESY, Hamburg. This was done at multiple energies and with different threshold settings for the sensors. Following these tests, the detector was used to collect data on cosmic muons, also with different threshold settings.

During the first analysis of the DESY-data it was found that there were multiple problems with the hardware. Hot lines, hot channels, malfunctioning chips and unstable channels bias the hit distributions by either adding lots of hits or adding hits inconstantly.

The DESY-data was used to investigate aforementioned problems. Some of the problems were able to be (partially) solved by masking parts of data. For other problems, suggestions of solutions have been given.

The hot channel problem has not been fixed. For now, all data in which these were present were excluded, if this was necessary. The hot lines were masked in the data, by selecting all lines with more than 100 pixels active. This is a temporary solution, since it will break down when more data is added. The bad channels have been masked if they were active less than 98.9% of the time. Additionally, some runs were excluded from the data. Malfunctioning chips were masked, since their behaviour is not trusted. The problem with the change of the position of the hot triangles has not been dealt with. This effect could indicate problems with the read-out of the sensors. Finally, the masking of the data was done for multiple runs, instead of single runs (as was done before).

Additionally to these problems with the sensors, runs were excluded from further data analysis. The runs that had no data, data missing or wrong threshold settings were marked. The synchronization of the Virtex-boxes seemed to cause problems in some runs; no fix has been found. Furthermore, it was found that the trigger-system had an efficiency lower than expected. This has also not been dealt with.

The selected data was used for further analysis. It was found that the masking of the data was a partial success, by noting that the energy resolution of the data improved for the 5.4 GeV data, but got worse for the other energies. However, the masking caused other functions, such as the longitudinal profiles, to function correctly once again. The linearity of the detector was found to be better on the masked data. Because of the mentioned reasons, we consider the masked data to be an improvement over the unmasked data.

More analysis on the data showed that the best energy resolution was obtained by filtering the data on HVP trigger and using past-future protection. The data of the individual sets (taken at different times) of the different energies were found to behave consistently, which means these data can be added together. The peaks of the longitudinal profile for different energies shifted in accordance with theory. The showers created by the incoming particle beam look to be well contained within the width of the detector. It was found that the highest number of showers surviving past-future protection per spill were obtained for higher beam intensities.

The data for different threshold values has been analysed by looking at the energy resolution and the clustersize. It was found that the best energy resolution was obtained for the data with the low-threshold setting (2×10^{-5}). The highest signal-to-noise ratio was obtained for the high-threshold setting (5×10^{-6}). The number of real hits in the detector remained approximately constant over the noise threshold used in the software.

Using the data on the cosmic muons, it was found that the clustersize was highest with the low-threshold setting and lowest with the high-threshold setting. No relation has been found between the threshold setting and the percentage of clusters that were not found by the tracking software.

We conclude that, even though a lot of problems were found, the detector is functioning as desired. The problems stated above usually occur only very infrequently and do not need to be looked at individually. The different settings for the noise threshold in the hardware and software are the most likely candidates to improve the energy resolution of the detector.

Chapter 8

Recommendations

The trigger system of the detector needs to be reevaluated and possibly adjusted. The current problem is that some particles are not detected. One could try to ignore the trigger-stream information in the data, and check on a frame-by-frame basis if this frame has been triggered or not. This relies on the fact that the number of hits in a frame with shower should be significantly higher than in a frame without shower. However, if this is done, a selection on the data is done beforehand. This is undesired, since important data could be lost. The best option would be to check the performance of the scintillation counters and possibly make adjustments. However, this might prove to be difficult as well.

Using the same method as above, the problems with the hot lines and hot channels can be removed when in each frame a quality check will be performed. This simply implies that the hits of all the sensors that have neighboring hits would be added together and a check would be made whether this value is below a certain threshold. This value would be different for every energy-level. Again, if one would want to implement this procedure, much care has to be taken. It is very easy to make errors here and lose data.

The different settings for the threshold (both in the hardware and the software) are the most likely candidate for improvements on the energy resolution. Beam tests at PS and SPS will be done in the near future. These tests might be good opportunities to investigate this possibility. The recommendation is to take a much larger range of settings. It would be most interesting to see how the system reacts to very low and very high threshold settings.

Bibliography

[1] A. Apostolou, *Data analysis from the beam test at DESY for the FoCal prototype*. Master thesis (Utrecht University), UU(SAP)13-9 2013.

[2] *The Great Soviet Encyclopedia: Cosmic rays*, 1979.

[3] H. Bichel, D.E. Groom and S.R. Klein, *Passage of particles through matter*. Particle Data Group, 2012.

[4] G. Eigen, *Phys341 Selected topics in particle physics: Transparencies for chapter IIa and IIb*. `http://web.ift.uib.no/~eigen/Phys232-02.pdf` (accesed 14-06-2014).

[5] E.M. Henley and A. García, *Subatomic Physics*. World Scientific, 3rd Edition, 2012.

[6] *Schematic of a particle shower*, `http://en.wikipedia.org/wiki/File:Schematic_of_a_particle_shower.svg` (accesed 14-06-2014)

[7] R. Turchetta, J.D. Berst, B. Casadei, G. Claus, C. Colledani, W. Dulinski, Y. Hu, D. Husson, J.P. Le Normand, J.L. Riester, G. Deptuch, U. Goerlach, S. Higueret, and M. Winter, *A monilithic active pixel sensor for charged particle tracking and imaging using standard VLSI CMOS tech-nology*. Nuclear Instruments and Methods in Physics Research A, 2001.

[8] A. Besson, *Development of CMOS Pixel sensors (CPS) for vertex detectors in present and future collider experiments*. 14th ICATPP Conference, 2013.

[9] E. Rocco, *Presentation: Foward Calorimeter (FoCal) for ALICE*. Jamboree, 2012.

[10] N. Deelen, *Tuning the FoCal prototype detector with cosmic muons*. Bachelor thesis (Utrecht University), UU(SAP)13-13 2013.

[11] R. Nusselder, *FoCal chip calibration with cosmic rays*. Bachelor thesis (Utrecht University), 2014.

[12] D. Fehlker, J. Alme, A. van den Brink, A.P. de Haas, G.J. Nooren, M. Reicher, D. Röhrich, M. Rossewij, K. Ullaland, and S. Yang, *Electronics for a highly segmented electromagnetic calorimeter prototype*. Journal of Instrumentation, 2013.

[13] A. van den Brink, *Drawings for ALICE*.

[14] *Safety Briefing for DESY Test Beam Users (31-01-2014)*, `http://testbeam.desy.de/e130574/e130575/e131129/DESY_Testbeam_Safety_20140131.pdf` (accesed 16-06-2014).

[15] E. Longo and I. Sestilli, 1975.

Appendix A

DESY Runs

Table A.1: The overview of all the runs taken at DESY. PPF = past-future protection. HVP = all events which had a HVP trigger attached.

Run	Energy (GeV)	Spills	No PFP	PFP	PFP and HVP	Threshold	Use this run for:	Comments
1	1.0	0	0	0	0	Old	0	Started data-taking: 10/02/2014 / Empty
2	1.0	1	0	0	0	Old	0	
3	1.0	1	108	28	13	Old	0	Runs 1-28 have the old threshold settings
4	1.0	1	1374	41	4	Old	0	In runs 1-28 changes to the beam were done
5	5.0	1	97	59	6	Old	0	
6	5.0	1	14	14	2	Old	0	
7	5.0	4	28	26	5	Old	0	
8	5.0	1	0	0	0	Old	0	
9	0.0	0	0	0	0	Old	0	Empty
10	5.0	16	165	150	29	Old	0	
11	0.0	2	0	0	0	Old	0	
12	5.0	15	164	152	40	Old	0	
13	5.0	16	192	178	38	Old	0	
14	0.0	1	0	0	0	Old	0	
15	5.0	15	173	141	23	Old	0	

16	5.0	15	178	167	31	Old	0	
17	0.0	1	0	0	0	Old	0	
18	5.0	18	233	201	44	Old	0	
19	5.0	5	1645	114	24	Old	0	
20	5.0	3	764	75	18	Old	0	
21	5.0	2	36	32	7	Old	0	
22	5.4	1	27	25	8	Old	0	
23	5.6	2	97	51	7	Old	0	
24	5.4	1	22	14	0	Old	0	
25	5.4	1	84	34	7	Old	0	
26	5.4	1	41	25	8	Old	0	
27	5.0	1	75	40	9	Old	0	
28	5.4	7	265	164	54	Old	0	
29	5.4	17	524	355	81	Normal	5.4 - Set 1	New threshold settings loaded
30	5.4	18	570	393	94	Normal	5.4 - Set 1	
31	0.0	2	0	0	0	Normal	Pedestal - Normal	
32	5.4	18	571	370	99	Normal	5.4 - Set 1	
33	5.4	17	528	359	87	Normal	5.4 - Set 1	
34	0.0	1	0	0	0	Normal	Pedestal - Normal	
35	5.4	19	576	378	104	Normal	5.4 - Set 1	
36	5.4	18	591	377	98	Normal	5.4 - Set 1	
37	0.0	1	0	0	0	Normal	Pedestal - Normal	
38	5.4	15	508	333	90	Normal	5.4 - Set 1	
39	5.4	19	543	388	103	Normal	5.4 - Set 1	
40	0.0	1	0	0	0	Normal	Pedestal - Normal	
41	5.4	20	545	341	79	Normal	5.4 - Set 1	
42	5.4	20	632	436	105	Normal	5.4 - Set 1	
43	0.0	1	0	0	0	Normal	Pedestal - Normal	
44	5.4	19	645	418	106	Normal	5.4 - Set 1	
45	5.4	10	341	222	50	Normal	5.4 - Set 1	
46	0.0	1	0	0	0	Normal	0	Run has incomplete data
47	5.4	2	39	27	3	Normal	5.4 - Set 1	
48	0.0	2	0	0	0	Normal	Pedestal - Normal	

49	5.4	9	307	196	54	Normal	5.4 - Set 1	
50	2.0	1	68	46	7	Normal	2.0 - Normal - Set 1	
51	2.0	24	1130	882	172	Normal	0	Run has incomplete data
52	2.0	39	1838	1433	282	Normal	2.0 - Normal - Set 1	
53	2.0	23	593	490	99	Normal	2.0 - Normal - Set 1	
54	0.0	2	0	0	0	Normal	Pedestal - Normal	
55	2.0	1	90	52	10	Normal	2.0 - Normal - Set 2	
56	2.0	19	1997	1158	238	Normal	2.0 - Normal - Set 2	
57	2.0	22	2436	1431	318	Normal	2.0 - Normal - Set 2	
58	2.0	29	3411	1849	392	Normal	2.0 - Normal - Set 2	
59	0.0	1	0	0	0	Normal	Pedestal - Normal	
60	2.0	82	9642	5243	1140	Normal	2.0 - Normal - Set 2	
61	0.0	2	0	0	0	Normal	Pedestal - Normal	
62	2.0	19	2130	1215	271	Normal	2.0 - Normal - Set 2	
63	2.0	24	2935	1599	366	Low	2.0 - Low - Set 1	New threshold settings loaded
64	0.0	1	0	0	0	Low	Pedestal - Low	
65	2.0	24	2791	1568	337	Low	2.0 - Low - Set 1	
66	2.0	23	2653	1545	358	Low	2.0 - Low - Set 1	
67	0.0	1	0	0	0	Low	Pedestal - Low	
68	2.0	24	2873	1541	348	Low	2.0 - Low - Set 1	
69	2.0	24	2732	1481	304	Low	2.0 - Low - Set 1	
70	0.0	1	0	0	0	Low	Pedestal - Low	
71	2.0	23	2743	1470	302	Low	0	Has a hot line
72	2.0	25	2842	1551	311	Low	2.0 - Low - Set 1	
73	0.0	1	0	0	0	Low	Pedestal - Low	
74	2.0	20	2312	1284	274	Low	2.0 - Low - Set 1	
75	2.0	1	107	65	20	High	2.0 - High - Set 1	New threshold settings loaded
76	0.0	1	0	0	0	High	Pedestal - High	
77	2.0	21	2216	1187	256	High	2.0 - High - Set 1	
78	2.0	18	2128	1183	260	High	2.0 - High - Set 1	
79	0.0	1	0	0	0	High	Pedestal - High	
80	2.0	5	474	249	55	High	2.0 - High - Set 1	
81	2.0	1	5357	10	1	High	0	Parasetic + bad channels

82	2.0	0	0	0	0	High	0	Run has no data
83	0.0	1	0	0	0	High	Pedestal - High	
84	0.0	0	0	0	0	Normal	0	Run has no data
85	4.0	2	31	23	4	Normal	0	Special run with different collimator
86	4.0	1	66	36	10	Normal	4.0 - Set 1	
87	4.0	2	33	29	7	Normal	4.0 - Set 1	
88	4.0	11	249	213	64	Normal	4.0 - Set 1	
89	4.0	19	389	331	92	Normal	4.0 - Set 1	
90	0.0	1	0	0	0	Normal	Pedestal - Normal	
91	4.0	15	315	275	61	Normal	4.0 - Set 1	
92	4.0	10	190	172	48	Normal	4.0 - Set 1	Computer had problems with memory
93	0.0	1	0	0	0	Normal	0	Run is excluded because of bad channels
94	4.0	7	149	130	33	Normal	4.0 - Set 1	
95	4.0	23	443	373	92	Normal	4.0 - Set 1	
96	0.0	1	0	0	0	Normal	Pedestal - Normal	
97	4.0	24	460	382	97	Normal	4.0 - Set 1	
98	4.0	23	430	371	95	Normal	4.0 - Set 1	
99	0.0	1	0	0	0	Normal	Pedestal - Normal	
100	4	22	402	343	93	Normal	4.0 - Set 1	
101	4	20	417	349	92	Normal	4.0 - Set 1	
102	5	1	259	27	5	Normal	0	Trigger inputs changed (Bit 2 now F)
103	0	1	0	0	0	Normal	Pedestal - Normal	
104	3	1	70	47	13	Normal	0	Starting up (different slit settings)
105	3	1	58	40	11	Normal	0	Starting up (different slit settings)
106	3	22	1468	886	232	Normal	3.0 - Set 1	
107	3	27	1997	1190	335	Normal	3.0 - Set 1	
108	0	1	0	0	0	Normal	Pedestal - Normal	
109	3	23	1669	1028	259	Normal	3.0 - Set 1	
110	3	27	1973	1204	309	Normal	3.0 - Set 1	
111	0	3	0	0	0	Normal	Pedestal - Normal	
112	3	24	1694	1028	265	Normal	3.0 - Set 1	
113	3	21	1456	896	217	Normal	3.0 - Set 1	
114	0	1	0	0	0	Normal	Pedestal - Normal	

115	3	24	1677	1064	281	Normal	3.0 - Set 1	
116	3	23	1530	966	251	Normal	3.0 - Set 1	
117	0	1	0	0	0	Normal	Pedestal - Normal	
118	3	23	1537	929	223	Normal	3.0 - Set 1	
119	3	11	568	358	85	Normal	3.0 - Set 1	
120	0	4	0	0	0	Normal	Pedestal - Normal	
121	0	5	1	1	0	Normal	0	Run is excluded because of bad channels
122	5.4	1	26	19	9	Normal	5.4 - Set 2	
123	5.4	22	455	336	93	Normal	5.4 - Set 2	
124	5.4	23	387	304	94	Normal	5.4 - Set 2	
125	0	1	1	1	0	Normal	Pedestal - Normal	
126	5.4	22	402	318	92	Normal	5.4 - Set 2	
127	5.4	22	396	312	86	Normal	5.4 - Set 2	
128	0	1	0	0	0	Normal	Pedestal - Normal	
129	5.4	21	392	299	69	Normal	5.4 - Set 2	
130	5.4	21	366	274	77	Normal	5.4 - Set 2	
131	0	1	0	0	0	Normal	Pedestal - Normal	
132	5.4	21	391	295	67	Normal	5.4 - Set 2	
133	5.4	20	346	264	82	Normal	5.4 - Set 2	
134	0	1	0	0	0	Normal	Pedestal - Normal	
135	5.4	16	271	218	57	Normal	5.4 - Set 2	
136	0	1	1	1	0	Normal	Pedestal - Normal	
137	0	1	3	3	0	Normal	Pedestal - Normal	
138	2	1	49	35	6	High	2.0 - High - Set 2	New threshold settings loaded
139	2	42	2356	1711	367	High	2.0 - High - Set 2	
140	2	21	1127	818	185	High	0	Has a hot line
141	0	1	0	0	0	High	Pedestal - High	
142	2	18	983	695	134	High	2.0 - High - Set 2	
143	2	20	1087	809	194	High	2.0 - High - Set 2	
144	0	1	1	1	0	High	Pedestal - High	
145	2	21	1134	819	189	High	2.0 - High - Set 2	
146	2	14	792	566	126	High	2.0 - High - Set 2	
147	0	1	0	0	0	High	Pedestal - High	

148	4	1	30	27	2	High	0	Still on high-threshold
149	4	1	49	26	6	Normal	4.0 - Set 2	New threshold settings loaded
150	0	1	0	0	0	Normal	Pedestal - Normal	
151	4	8	330	236	61	Normal	4.0 - Set 2	
152	4	53	2170	1545	406	Normal	4.0 - Set 2	
153	0	1	0	0	0	Normal	0	Run has incomplete data
154	4	21	828	610	148	Normal	4.0 - Set 2	
155	4	20	817	588	166	Normal	4.0 - Set 2	
156	0	1	0	0	0	Normal	Pedestal - Normal	
157	5.4	1	26	17	3	Normal	5.4 - Set 3	
158	5.4	22	596	411	122	Normal	5.4 - Set 3	
159	5.4	25	656	450	120	Normal	5.4 - Set 3	
160	0	1	0	0	0	Normal	Pedestal - Normal	
161	5.4	23	659	429	114	Normal	5.4 - Set 3	
162	5.4	21	589	419	111	Normal	5.4 - Set 3	
163	0	1	0	0	0	Normal	Pedestal - Normal	
164	5.4	22	605	431	122	Normal	5.4 - Set 3	
165	5.4	26	756	514	148	Normal	5.4 - Set 3	
166	0	1	0	0	0	Normal	Pedestal - Normal	
167	5.4	21	603	416	112	Normal	5.4 - Set 3	
168	5.4	13	341	228	49	Normal	5.4 - Set 3	
169	0	2	0	0	0	Normal	Pedestal - Normal	
170	0	1	1	1	0	Normal	Pedestal - Normal	Stopped data-taking: 17/02/2014

Appendix B

MUON Runs

Table B.1: The overview of all MUON data used in this thesis.

Run	Spills	Mode	Threshold	Use this run for:	Comments
547	246	Cosmic	Normal	Cosmic - Normal	Started data-taking: 20/02/2014
548	6	Ped	Normal	Pedestal - Normal	
549	71	Cosmic	Normal	Cosmic - Normal	
550	8	Ped	Normal	Pedestal - Normal	
551	916	Cosmic	Normal	Cosmic - Normal	
552	5	Ped	Normal	Pedestal - Normal	
553	5	Ped	Low	Pedestal - Low	
554	4500	Cosmic	Low	Cosmic - Low	
555	5	Ped	Low	Pedestal - Low	
556	3809	Cosmic	Low	Cosmic - Low	
557	5	Ped	Low	Pedestal - Low	
558	65	Ped	Normal	Pedestal - Normal	
559	214	Cosmic	Normal	Cosmic - Normal	
560	4	Ped	Normal	Pedestal - Normal	
561	125	Cosmic	Normal	Cosmic - Normal	Computer crashed during run
562	238	Cosmic	Normal	Cosmic - Normal	
563	7	Ped	Normal	Pedestal - Normal	
564	419	Cosmic	Normal	Cosmic - Normal	
565	5	Ped	Normal	Pedestal - Normal	
566	5	Ped	High	Pedestal - High	
567	990	Cosmic	High	Cosmic - High	
568	5	Ped	High	Pedestal - High	
569	132	Cosmic	High	Cosmic - High	
570	3	Ped	High	Pedestal - High	
571	5	Ped	High	Pedestal - High	Computer memory added
572	287	Cosmic	High	Cosmic - High	
573	1	Ped	High	Pedestal - High	
574	999	Cosmic	High	Cosmic - High	
575	4	Ped	High	Pedestal - High	
576	1003	Cosmic	High	Cosmic - High	
577	5	Ped	High	Pedestal - High	
578	419	Cosmic	High	Cosmic - High	
579	5	Ped	High	Pedestal - High	
580	317	Cosmic	High	Cosmic - High	
581	6	Ped	High	Pedestal - High	

582	349	Cosmic	High	Cosmic - High	
583	7	Ped	High	Pedestal - High	
584	477	Cosmic	High	Cosmic - High	
585	3	Ped	High	Pedestal - High	
586	1752	Cosmic	High	Cosmic - High	
587	4	Ped	High	Pedestal - High	
588	42	Cosmic	High	Cosmic - High	
589	1	Ped	High	Pedestal - High	
590	252	Cosmic	High	Cosmic - High	
591	5	Ped	High	Pedestal - High	
592	1	Ped	High	Pedestal - High	
593	366	Cosmic	High	Cosmic - High	
594	1	Ped	High	Pedestal - High	
595	1475	Cosmic	High	Cosmic - High	
596	300	Cosmic	High	Cosmic - High	Testing sensors with chipscope
597	264	Cosmic	High	Cosmic - High	
598	2080	Cosmic	High	Cosmic - High	OS was updated
599	2	Ped	High	Pedestal - High	
600	83	Cosmic	High	Cosmic - High	
601	0	Ped	High	0	Run is empty
602	5	Ped	Normal	Pedestal - Normal	
603	354	Cosmic	Normal	Cosmic - Normal	
604	5	Ped	Normal	Pedestal - Normal	
605	354	Cosmic	Normal	Cosmic - Normal	
606	9	Ped	Normal	Pedestal - Normal	
607	2013	Cosmic	Normal	Cosmic - Normal	
608	17	Ped	Normal	Pedestal - Normal	
609	53	Cosmic	Normal	Cosmic - Normal	Stopped data-taking: 22/04/2014

Appendix C

Threshold settings

Table C.1: VREF1/VREF2 values for the normal-threshold setting (noise level of 10^{-5})

Sensor	VREF1	VREF2	Sensor	VREF1	VREF2	Sensor	VREF1	VREF2
0	82	84	32	142	81	64	150	80
1	121	80	33	153	50	65	143	80
2	147	80	34	132	82	66	243	76
3	155	82	35	189	78	67	100	80
4	146	80	36	141	77	68	166	77
5	146	85	37	171	81	69	210	75
6	135	80	38	174	82	70	121	83
7	117	77	39	147	78	71	147	75
8	169	79	40	159	80	72	165	84
9	170	81	41	128	86	73	165	80
10	150	85	42	139	80	74	98	91
11	167	83	43	143	78	75	106	82
12	176	82	44	112	81	76	150	80
13	150	80	45	130	82	77	203	75
14	159	79	46	97	83	78	162	78
15	158	75	47	138	78	79	114	83
16	120	82	48	146	85	80	126	82
17	107	85	49	127	77	81	140	81
18	160	76	50	170	76	82	180	79
19	150	78	51	150	80	83	111	84
20	180	76	52	198	83	84	163	75
21	140	75	53	123	82	85	140	76
22	153	77	54	158	80	86	158	73
23	164	79	55	148	84	87	143	77
24	155	80	56	150	75	88	161	82
25	150	80	57	156	76	89	159	80
26	150	80	58	158	82	90	157	79
27	175	75	59	159	81	91	171	86
28	141	80	60	138	80	92	85	85
29	156	81	61	230	80	93	178	76
30	144	82	62	128	84	94	146	84
31	109	76	63	145	88	95	124	84

Table C.2: VREF1/VREF2 values for the high-threshold setting (noise level of 5×10^{-6})

Sensor	VREF1	VREF2	Sensor	VREF1	VREF2	Sensor	VREF1	VREF2
0	80	84	32	140	81	64	147	80
1	119	80	33	151	50	65	143	80
2	144	80	34	128	82	66	240	76
3	152	82	35	187	78	67	150	80
4	144	80	36	138	77	68	163	77
5	143	85	37	168	81	69	207	75
6	132	80	38	170	82	70	119	83
7	115	77	39	147	78	71	144	75
8	166	79	40	157	80	72	162	84
9	166	81	41	126	86	73	162	80
10	147	85	42	137	80	74	98	91
11	163	83	43	141	78	75	103	82
12	174	82	44	108	81	76	147	80
13	147	80	45	128	82	77	200	75
14	156	79	46	100	83	78	161	78
15	155	75	47	136	78	79	110	83
16	117	82	48	143	85	80	124	82
17	101	85	49	124	77	81	137	81
18	157	76	50	168	76	82	178	79
19	147	78	51	147	80	83	109	84
20	177	76	52	195	83	84	160	75
21	130	75	53	120	82	85	138	76
22	150	77	54	155	80	86	155	73
23	161	79	55	143	84	87	140	77
24	148	74	56	148	75	88	158	82
25	147	80	57	153	75	89	157	80
26	148	80	58	158	82	90	154	79
27	172	75	59	155	81	91	169	86
28	138	80	60	135	80	92	83	85
29	153	81	61	228	80	93	176	76
30	142	82	62	125	84	94	144	84
31	112	76	63	145	88	95	121	84

Table C.3: VREF1/VREF2 values for the low-threshold setting (noise level of 2×10^{-5})

Sensor	VREF1	VREF2	Sensor	VREF1	VREF2	Sensor	VREF1	VREF2
0	84	84	32	145	81	64	152	80
1	124	80	33	156	50	65	140	80
2	149	80	34	135	82	66	243	76
3	158	82	35	192	78	67	150	80
4	149	80	36	143	77	68	169	77
5	148	85	37	173	81	69	212	75
6	137	80	38	176	82	70	124	83
7	120	77	39	150	78	71	150	75
8	172	79	40	162	80	72	165	84
9	172	81	41	131	86	73	167	80
10	153	85	42	142	80	74	98	91
11	169	83	43	145	78	75	109	82
12	178	82	44	114	81	76	152	80
13	152	80	45	134	82	77	205	75
14	161	79	46	94	83	78	164	78
15	160	75	47	141	78	79	120	83
16	122	82	48	149	85	80	129	82
17	109	85	49	129	77	81	142	81
18	162	76	50	173	76	82	182	79
19	153	78	51	152	80	83	113	84
20	183	76	52	200	83	84	166	75
21	143	75	53	125	82	85	145	76
22	155	77	54	160	80	86	160	73
23	167	79	55	150	84	87	145	77
24	152	74	56	152	75	88	163	82
25	152	80	57	158	75	89	161	80
26	152	80	58	160	82	90	160	79
27	177	75	59	159	81	91	173	86
28	143	80	60	140	80	92	88	85
29	158	81	61	232	80	93	181	76
30	146	82	62	131	84	94	149	84
31	116	76	63	145	88	95	124	84

Appendix D

Voltage scintillation counters

Table D.1: Present

Voltage [V]	Counts
1700	860
1750	5189
1800	6214
1820	6617
1840	6415
1850	6695
1860	6732
1900	7424
1950	13194

Table D.2: Horizontal

Voltage [V]	Counts
600	151
700	2055
760	1887
800	2065
860	1976
900	2043
960	2084
1000	2041
1060	2218
1100	2424

Table D.3: Vertical

Voltage [V]	Counts
1000	687
1100	2704
1200	2594
1260	2777
1300	2689
1360	2774
1400	2859
1500	2893
1560	3123
1600	3432
1700	5432

Table D.4: Front

Voltage [V]	Counts
1600	982
1640	2835
1650	5088
1660	5894
1680	6360
1700	6066
1720	6095
1760	5625
1800	5893
1820	5710
1860	6392
1900	10326

Table D.5: Back

Voltage [V]	Counts
1700	0
1800	171
1900	689

Appendix E

Mask overview

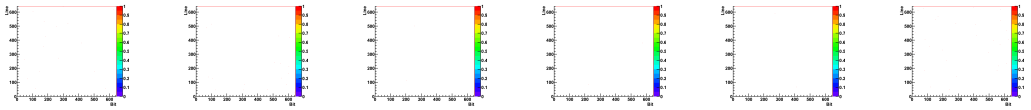
Sensor: 0

Sensor: 1

Sensor: 2

Sensor: 3

Sensor: 4

Sensor: 5

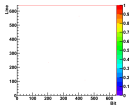
Sensor: 6

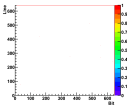
Sensor: 7

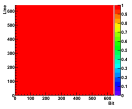
Sensor: 8

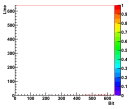
Sensor: 9

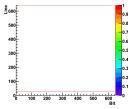
Sensor: 10

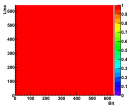
Sensor: 11

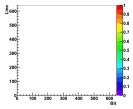
Sensor: 12

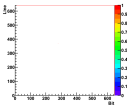
Sensor: 13

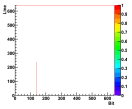
Sensor: 14

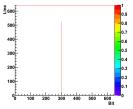
Sensor: 15

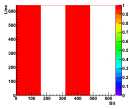
Sensor: 16

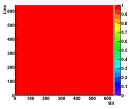
Sensor: 17

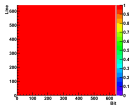
Sensor: 18

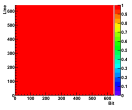
Sensor: 19

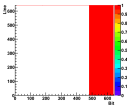
Sensor: 20

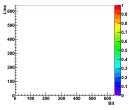
Sensor: 21

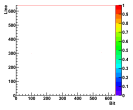
Sensor: 22

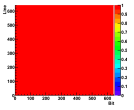
Sensor: 23

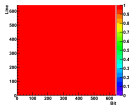
Sensor: 24

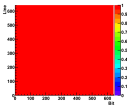
Sensor: 25

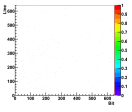
Sensor: 26

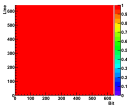
Sensor: 27

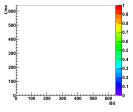
Sensor: 28

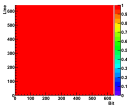
Sensor: 29

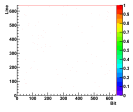
Sensor: 30

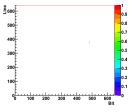
Sensor: 31

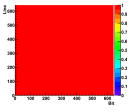
Sensor: 32

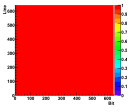
Sensor: 33

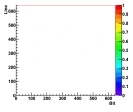
Sensor: 34

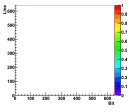
Sensor: 35

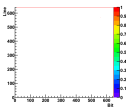
Sensor: 36

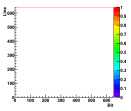
Sensor: 37

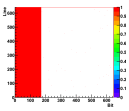
Sensor: 38

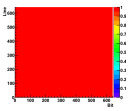
Sensor: 39

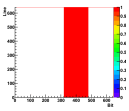
Sensor: 40

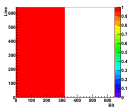
Sensor: 41

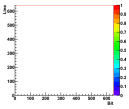
Sensor: 42

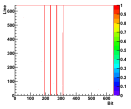
Sensor: 43

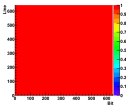
Sensor: 44

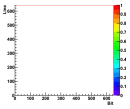
Sensor: 45

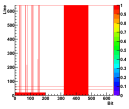
Sensor: 46

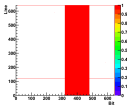
Sensor: 47

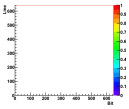
Sensor: 48

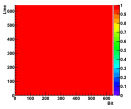
Sensor: 49

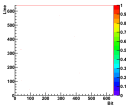
Sensor: 50

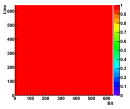
Sensor: 51

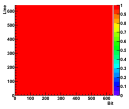
Sensor: 52

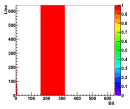
Sensor: 53

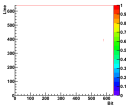
Sensor: 54

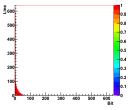
Sensor: 55

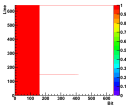
Sensor: 56

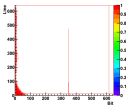
Sensor: 57

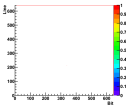
Sensor: 58

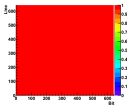
Sensor: 59

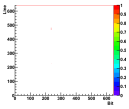
Sensor: 60

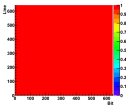
Sensor: 61

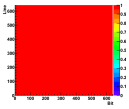
Sensor: 62

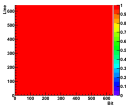
Sensor: 63

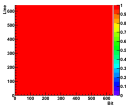
Sensor: 64

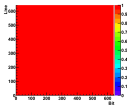
Sensor: 65

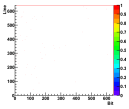
Sensor: 66

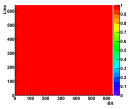
Sensor: 67

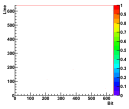
Sensor: 68

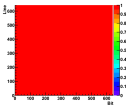
Sensor: 69

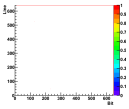
Sensor: 70

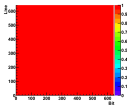
Sensor: 71

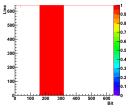
Sensor: 72

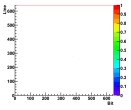
Sensor: 73

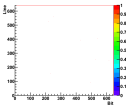
Sensor: 74

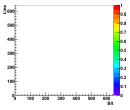
Sensor: 75

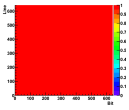
Sensor: 76

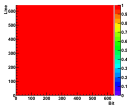
Sensor: 77

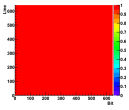
Sensor: 78

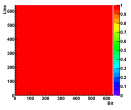
Sensor: 79

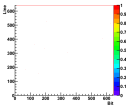
Sensor: 80

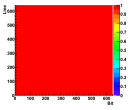
Sensor: 81

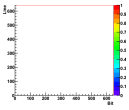
Sensor: 82

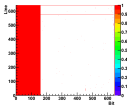
Sensor: 83

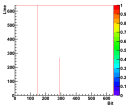
Sensor: 84

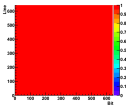
Sensor: 85

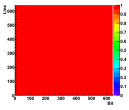
Sensor: 86

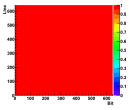
Sensor: 87

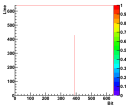
Sensor: 88

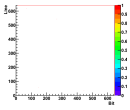
Sensor: 89

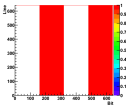
Sensor: 90

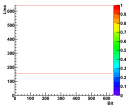
Sensor: 91

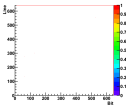
Sensor: 92

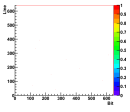
Sensor: 93

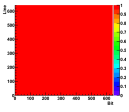
Sensor: 94

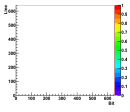
Sensor: 95